Cancer Cell

Article

CDKN2A deletion remodels lipid metabolism to prime glioblastoma for ferroptosis

Graphical abstract

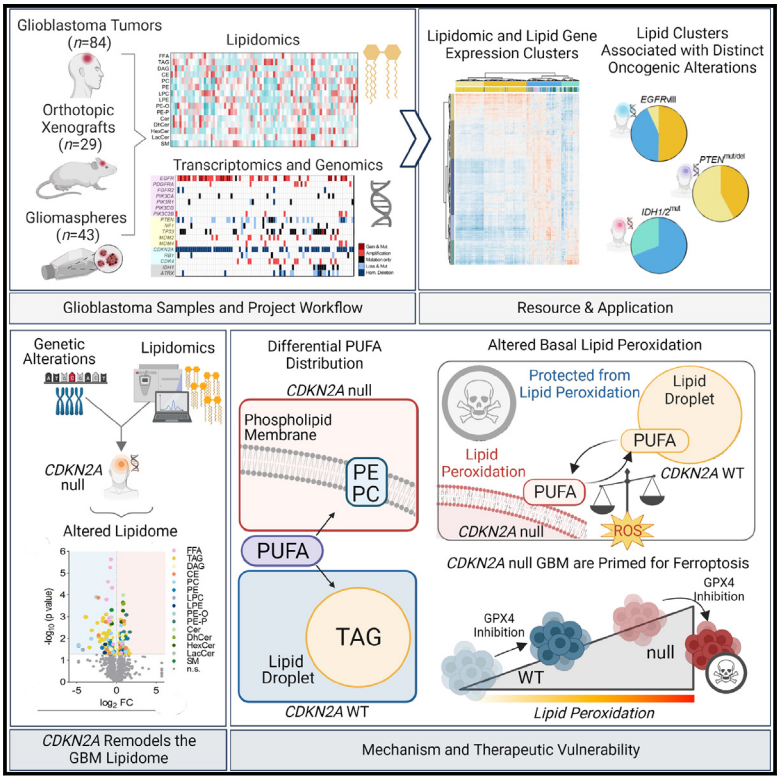

Highlights

- Molecular and lipidomic resource of over 150 GBM tumors and derivative models
- Unbiased multi-omic analysis identifies CDKN2A as a regulator of lipid metabolism
- *CDKN2A* deletion reduces oxidizable PUFA sequestration into lipid droplets
- GBMs with *CDKN2A* deletion are susceptible to lipid peroxidation and ferroptosis

Authors

Jenna K. Minami, Danielle Morrow, Nicholas A. Bayley, ..., Scott J. Dixon, Steven J. Bensinger, David A. Nathanson

Correspondence

sjdixon@stanford.edu (S.J.D.), sbensinger@mednet.ucla.edu (S.J.B.), dnathanson@mednet.ucla.edu (D.A.N.)

In brief

Minami et al. integrate lipidomic, transcriptomic, and genomic profiling data to identify altered lipid metabolism in *CDKN2A*-deleted glioblastoma (GBM). *CDKN2A* deletion remodels the distribution of polyunsaturated fatty acids into different lipid compartments, sensitizing GBMs with *CDKN2A* loss to lipid peroxidation and ferroptosis *in vitro* and *in vivo.*

Minami et al., 2023, Cancer Cell *41*, 1048–1060
June 12, 2023
https://doi.org/10.1016/j.ccell.2023.05.001

CellPress

CellPress
OPEN ACCESS

Cancer Cell

Article

CDKN2A deletion remodels lipid metabolism to prime glioblastoma for ferroptosis

Jenna K. Minami,[1,8] Danielle Morrow,[1,8] Nicholas A. Bayley,[1,8] Elizabeth G. Fernandez,[1] Jennifer J. Salinas,[1] Christopher Tse,[1] Henan Zhu,[1] Baolong Su,[2] Rhea Plawat,[1] Anthony Jones,[1] Alessandro Sammarco,[2] Linda M. Liau,[3,7] Thomas G. Graeber,[1,7] Kevin J. Williams,[5,6] Timothy F. Cloughesy,[1,3,7] Scott J. Dixon,[4,*] Steven J. Bensinger,[1,2,5,7,*] and David A. Nathanson[1,7,9,*]

[1]Department of Molecular and Medical Pharmacology, University of California Los Angeles, Los Angeles, CA 90095, USA
[2]Department of Microbiology, Immunology and Molecular Genetics, University of California, Los Angeles, Los Angeles, CA 90095, USA
[3]Department of Neurology, David Geffen School of Medicine, University of California, Los Angeles, Los Angeles, CA, USA
[4]Department of Biology, Stanford University, Stanford, CA 94305, USA
[5]UCLA Lipidomics Core, University of California, Los Angeles, Los Angeles, CA 90095, USA
[6]Department of Biological Chemistry, University of California, Los Angeles, Los Angeles, CA 90095, USA
[7]Jonsson Comprehensive Cancer Center, David Geffen School of Medicine, University of California, Los Angeles, CA 90095, USA
[8]These authors contributed equally
[9]Lead contact
*Correspondence: sjdixon@stanford.edu (S.J.D.), sbensinger@mednet.ucla.edu (S.J.B.), dnathanson@mednet.ucla.edu (D.A.N.)
https://doi.org/10.1016/j.ccell.2023.05.001

SUMMARY

Malignant tumors exhibit heterogeneous metabolic reprogramming, hindering the identification of translatable vulnerabilities for metabolism-targeted therapy. How molecular alterations in tumors promote metabolic diversity and distinct targetable dependencies remains poorly defined. Here we create a resource consisting of lipidomic, transcriptomic, and genomic data from 156 molecularly diverse glioblastoma (GBM) tumors and derivative models. Through integrated analysis of the GBM lipidome with molecular datasets, we identify *CDKN2A* deletion remodels the GBM lipidome, notably redistributing oxidizable polyunsaturated fatty acids into distinct lipid compartments. Consequently, *CDKN2A*-deleted GBMs display higher lipid peroxidation, selectively priming tumors for ferroptosis. Together, this study presents a molecular and lipidomic resource of clinical and preclinical GBM specimens, which we leverage to detect a therapeutically exploitable link between a recurring molecular lesion and altered lipid metabolism in GBM.

INTRODUCTION

Molecular alterations in cancer rewire metabolism resulting in specific metabolic vulnerabilities that could be exploited for therapy.[1–5] Large-scale multi-omic studies in cancer cell lines have further advanced our understanding of the intersection between molecular diversity and metabolic heterogeneity, indicating distinct metabolic vulnerabilities may exist within defined molecular subsets of cancer.[6,7] However, the translatability of these findings into effective cancer treatments is potentially limited due to gaps in our understanding of the molecular and metabolic fidelity of conventional cell lines grown *in vitro*.[8–12] Thus, accounting for both the molecular diversity and environment of human tumors is crucial to identify translatable metabolic targets for patients with cancer.

Glioblastomas (GBMs) are universally lethal brain tumors that exhibit extensive genetic and transcriptional heterogeneity.[13,14] Specific oncogenic alterations (e.g., *EGFR* mutation and *IDH* mutation) reprogram aspects of GBM cellular lipid metabolism, uncovering potential opportunities to exploit altered tumor metabolism for GBM therapy.[15–19] Whether the diverse molecular landscape found in GBMs leads to heterogeneous lipidomic phenotypes and distinct metabolic vulnerabilities is unknown. Here, we developed a large library of molecularly annotated GBM tumors and derivative *in vitro* and *in vivo* orthotopic models to search for clinically relevant relationships between specific molecular lesions and lipid metabolic phenotypes.

RESULTS

A molecular and lipidomic resource of glioblastoma tumors and derivative preclinical models

84 tumors from patients with GBM were obtained from surgical resections and profiled using lipidomic, transcriptomic, and whole-exome sequencing methods (Figures 1A and S1A). We also analyzed 29 GBM orthotopic xenografts (PDXs) and 43 gliomasphere (GS) cell cultures derived from our GBM tumor cohort (Figure 1A). For each sample, shotgun lipidomics quantified up to 1,020 distinct lipid species from 15 lipid subclasses, revealing considerable variation in the lipidome across GBM tumors as well as the derivative models (Figures 1B and S1B). Genomic analysis demonstrated that our tumor sample cohort contained the molecular lesions within the core pathways known to be altered in GBMs (e.g., RTK/RAS/PI3K, P53, and RB signaling

CellPress
OPEN ACCESS

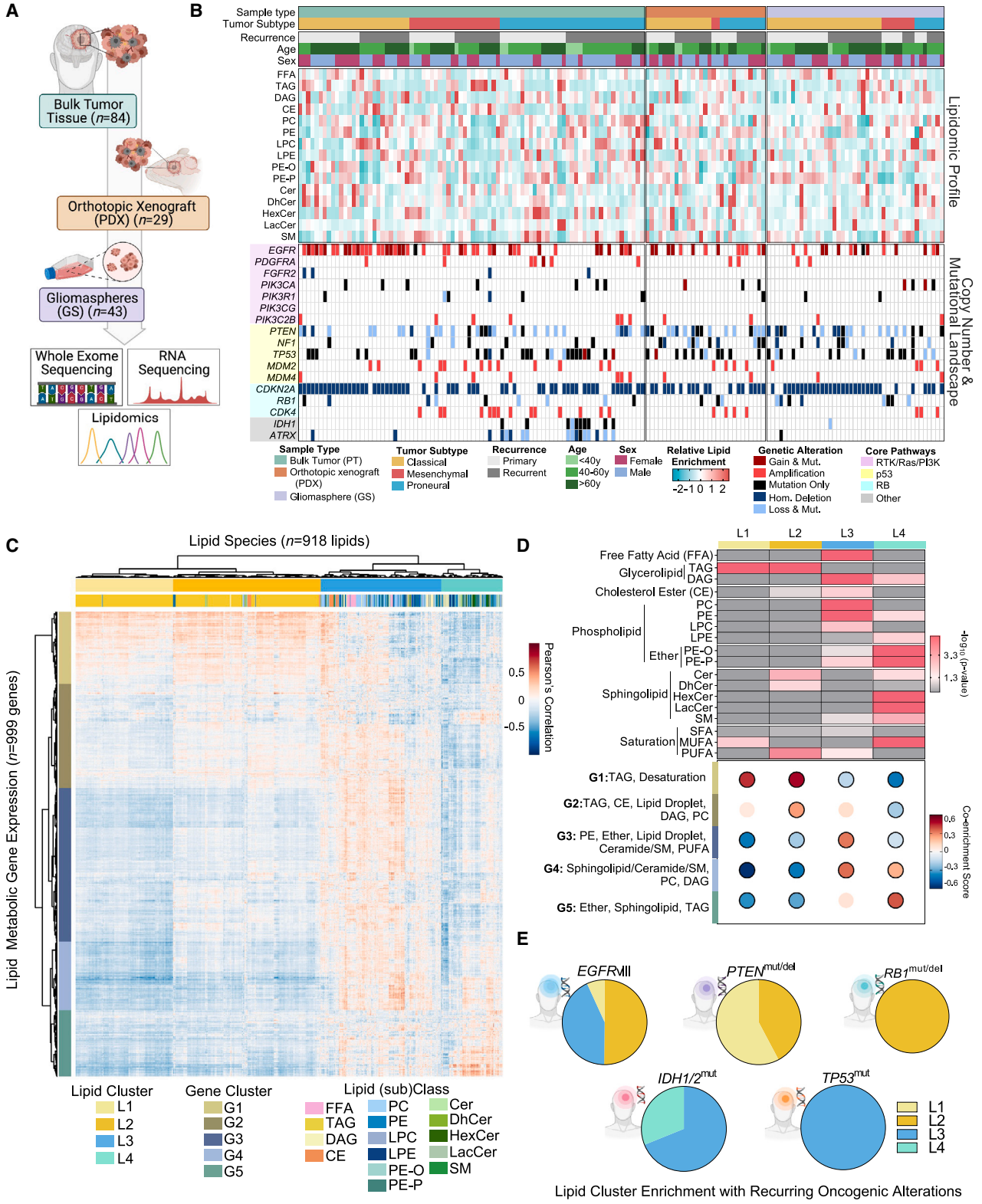

Figure 1. A molecular and lipidomic resource of glioblastoma tumors and derivative preclinical models

(A) Schematic representation of data collection workflow across glioblastoma (GBM) bulk tumor tissue (n = 84) and patient-derived models (orthotopic xenografts [n = 29] and gliomaspheres [n = 43]).

(legend continued on next page)

pathways)[13] and encompass diverse patient characteristics that include tumor transcriptional subtypes (classical, mesenchymal, proneural),[14] recurrence, age, gender, and ethnicity (Figures 1B and S1A). Likewise, our PDX and GS models recapitulate both the recurring genetic lesions and transcriptional subtypes of GBM tumors (Figure 1B). Together, this large collection of clinical and preclinical GBM specimens captures and highlights the heterogeneity across both the molecular and lipidomic landscape of GBM.

Lipids are structurally and functionally diverse molecules synthesized and regulated by multiple metabolic pathways and enzymes.[20] To explore whether the heterogeneity observed in the GBM lipidome is linked to variation in lipid metabolic gene expression programs, we correlated lipid species with the expression of lipid metabolism-related genes. Using our patient sample cohort, we found that lipid metabolic genes and lipid species clustered primarily into two groups separating triacylglycerides (TAGs) from other lipid species (Figures 1C and S2A). Lipid clusters within the TAG group further delineated monounsaturated (L1) and polyunsaturated (L2) TAGs, while clusters within the second group separated phospholipids (PC, PE), free fatty acids, and diacylglycerides (L3) from ether lipids and ceramides (L4) (Figures 1C, 1D, and S2A). Gene clusters showed strong correspondence with associated lipid classes including TAGs (G1, G2), phospholipids (G3, G4), ether lipids (G3, G5), and ceramides (G4, G5) based on Gene Ontology (GO) term enrichment. Moreover, GO terms related to acyl tail desaturation were enriched in gene clusters (G1, G3) that correlated with lipid groups containing polyunsaturated fatty acids (PUFA) (L2 and L3) (Figures 1D and S2B and Table S1). We conclude that specific differences in lipid metabolic gene expression found across the somatic landscape of GBM are associated with distinct lipid clusters containing species representing specific subclasses and fatty acid saturation states.

Next, to determine if specific oncogenic events align with distinct lipid metabolic clusters, we annotated the lipid species differentially abundant among previously defined oncogenic regulators of lipid metabolic reprogramming in GBM and/or other cancers (e.g., *IDH* mutation, *TP53* mutation, *EGFR*vIII mutation, *PTEN* deletion/mutation, *RB* mutation, *MDM2/4* amplification).[18,19,21–24] Among the various oncogenic lesions represented in our GBM tumor cohort, we found significant heterogeneity both in the number of lipids that differed and in their associated enrichment for specific lipid clusters (Figures 1E and S2C). For example, *IDH* mutant GBMs were enriched in lipid clusters containing phospholipids and MUFAs (L3 and L4) (Figures 1E and S2C). This result confirms recent findings.[18,19] Conversely, enriched lipids in *EGFR*vIII mutant GBMs consisted of TAGs and PUFAs (L2 cluster) in addition to phospholipids (L3 cluster). These observations support previous findings suggesting that mutant EGFR drives the synthesis of complex fatty acids containing PUFAs as well as phospholipids, both of which support oncogenic signaling.[16,22] Notably, the distinct lipid composition signatures that distinguish *IDH* and *EGFR* mutant tumors were mirrored in their respective enrichment patterns observed among the lipid gene clusters (Figure S2D). Collectively, these data demonstrate that the heterogeneity in the GBM lipidome may arise from the diversity in oncogenic alterations among individual tumors.

CDKN2A deletion alters the GBM lipidome

To identify cell intrinsic regulators of GBM lipid metabolism, we next performed a correlation analysis from our patient-derived GSs between the lipidome (n = 835 lipids) and protein-coding genes (n = 10,778 genes). Genes were filtered to remove transcripts with low expression levels, and both genes and lipid species were filtered to remove features with low variances (see STAR Methods). Hierarchical clustering of genes with the most variable correlations (n = 2,695 genes) identified two distinct gene-lipid groupings (Figure 2A, see STAR Methods). To examine whether specific genomic alterations were associated with these clusters, we scored individual samples for their cluster enrichment (Figure S3A) and then tested their association with gene-level somatic point mutations and locus-level copy number alterations (Figures 2B and S3B, see STAR Methods). While non-significant hits included mutant *RB1* and *TP53*, both of which drive tumor lipid metabolic reprogramming,[21,23] the only significant genetic alteration delineating these groups mapped to the chromosome 9p21 locus, the location of the tumor suppressor cyclin-dependent kinase inhibitor 2A (*CDKN2A*). RNA expression confirmed *CDKN2A* as the most differentially expressed transcript at this locus among our gene-lipid groups (Figure 2B). *CDKN2A*, deleted in nearly 60% of GBM tumors, encodes the p14/16 proteins that canonically regulate cell cycle and cell fate pathways.[25,26] To our knowledge, a role for *CDKN2A* in regulating lipid composition in cancer has not been reported.

Principal component analysis (PCA), followed by varimax rotation,[27] of all measured lipid species differentiated *CDKN2A* wild-type (WT) from *CDKN2A* null GSs along the first rotated component (Figure 2C). Compared with *CDKN2A* WT GSs, *CDKN2A* deletion was associated with significant changes in the levels of 195 individual lipid species distributed across 15 detectable lipid subclasses (Figure 2D), as well as all four of the lipid clusters we defined above (Figure 2E). Closer inspection of these differentially enriched lipids revealed distinct features of acyl tail utilization. Lipid species more abundant in *CDKN2A* WT

(B) Plot describing sample type, subtype, lipid composition (class % of total), copy number alterations and mutations in GBM, tumor recurrence, patient age, and gender. Lipid composition is plotted as a *Z*-score across samples within a tumor microenvironment type.
(C) Correlation matrix of lipid species (species % of total, n = 918 lipid species) and lipid-related gene expression (n = 999 genes) across GBM tumors.
(D) Lipid class and saturation enrichment for each lipid cluster (significance calculated by hypergeometric test against total lipidome with false discovery rate adjustment). Dot plot summarizes gene cluster-lipid cluster associations. Significant associations derived from Kolmogorov-Smirnov testing are outlined in black (see STAR Methods). Gene clusters are labeled with summarized interpretations of enriched Gene Ontology terms.
(E) Pie charts representing the log odds ratio scores of over-enriched lipid clusters for differentially abundant lipid species in altered samples relative to WT samples. See also Figures S1 and S2 and Table S1.
CE, cholesterol ester; Cer, ceramide; DAG, diacylglycerol; FFA, free fatty acid; DhCer, dihydroceramide; HexCer, hexosylceramide; LacCer, lactosylceramide; LPE, lysophosphatidylcholine; LPC, lysophosphatidylethanolamine; PC, phosphatidylcholine; PE, phosphatidylethanolamine; PE-O, alkyl-ether-linked phosphatidylethanolamine; PE-P, vinyl-ether-linked phosphatidylethanolamine; SM, sphingomyelin; TAG, triacylglyceride

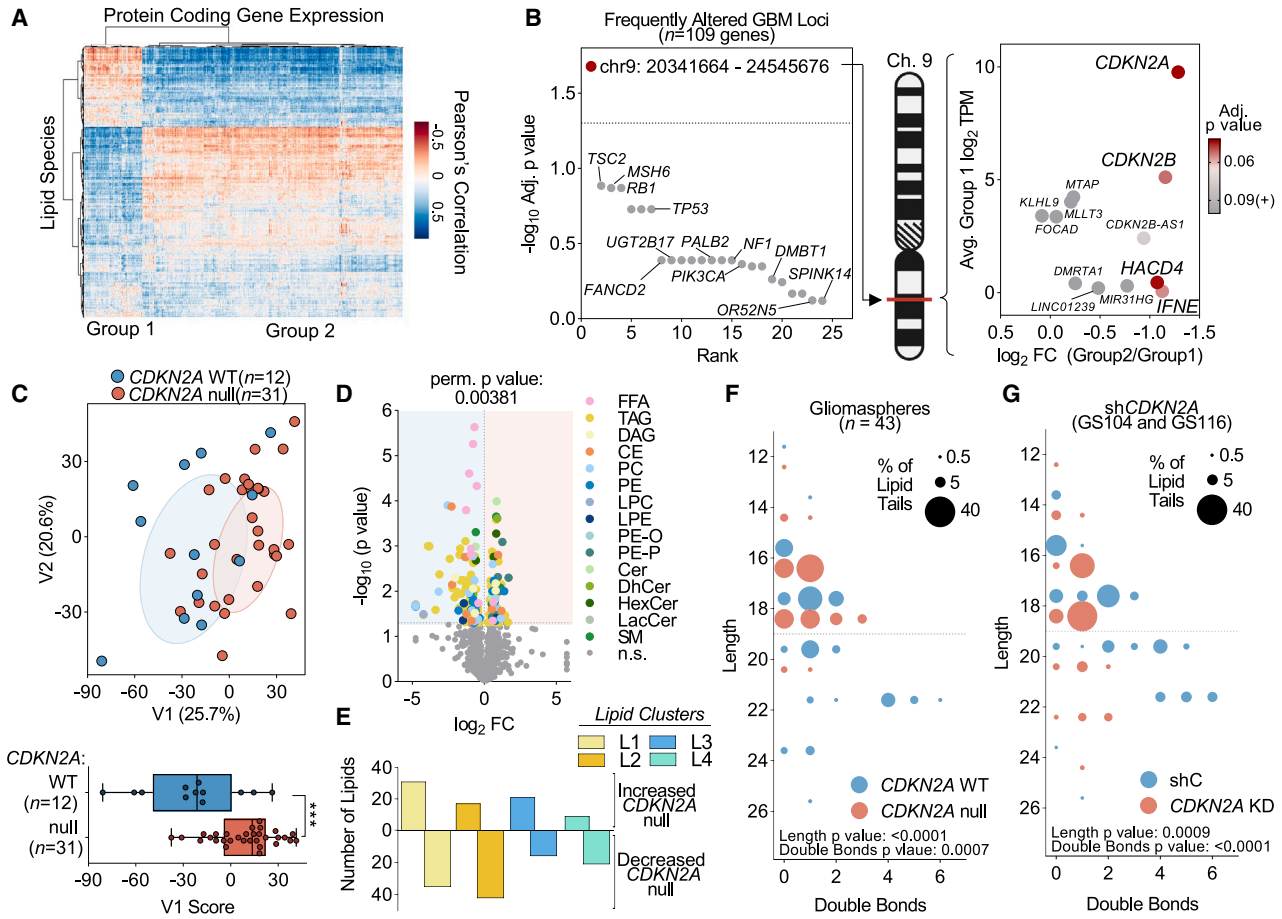

Figure 2. Comprehensive characterization of the GBM lipidome reveals the impact of *CDKN2A* deletion

(A) Correlation matrix of lipid composition (species % of class, n = 835) and gene expression of protein-coding genes (n = 2,695) in gliomaspheres (GSs) (n = 43).

(B) Scatterplot of gene- and locus-level somatic alterations (n = 24 somatic events covering 109 genes) ranked by their association with the gene set composite score (see STAR Methods). Scatterplot shows the average group 1 gene expression (log^2 TPM) and shrunken log_2 fold change (group 2/group 1) of genes at the chr9p21 locus identified. Shrunken fold changes and adjusted p values are from DESeq2 (see STAR Methods).

(C) Varimax rotated principal component analysis (V1, V2) of all lipids (species % of class, n = 985 species) between *CDKN2A* WT (blue, n = 12) and null (pink, n = 31) GSs. 50% data ellipses are shown. Quantification of difference in rotated component 1 scores between *CDKN2A* WT (n = 12) and null (n = 31) samples is shown. Boxplots depict the median, interquartile range, and extrema (significance calculated by Student's two-sample t test).

(D) Volcano plot of lipids (species % of class) altered by *CDKN2A* deletion in GSs. Significantly altered lipids are colored by species (Student's t test p value < 0.05). Permutation p value representing significance of differential abundance testing results is displayed (see STAR Methods).

(E) Number of lipid species altered with *CDKN2A* deletion binned by previously defined lipid clusters (see Figure 1).

(F) Acyl tail length and double bond characteristics of significantly altered lipid species identified in Figure 2D (significance calculated by Student's two-sample t test).

(G) Acyl tail length and double bond characteristics of significantly altered lipid species in CDKN2A WT GS (GS104 and GS116) infected with shRNA scramble control (shC) or two different shRNAs targeting *CDKN2A* (KD-1 and KD-2). Each of these shRNAs target both p14 and p16 from the *CDKN2A* locus (significance calculated by Student's two-sample t test). p > 0.05 = ns; p < 0.05 = *; p < 0.01 = **; p < 0.001 = ***; p < 0.0001 = ****. See also Figures S3 and S4.

GSs comprised acyl tails that were highly desaturated (i.e., polyunsaturated fatty acids or PUFAs) and greater than 20 carbons in length (i.e., very long chain fatty acids) (Figure 2F). By contrast, the lipid species enriched in *CDKN2A* null GSs were composed of generally shorter fatty acyls, including medium and long chain species (i.e., 12–18 carbons). Interestingly, these distinct lipidomic characteristics (i.e., desaturation state or acyl tail length) were not generalizable to the broader lipidomes of *CDKN2A* WT and null cells (Figures S3C and S3D), indicating that these characteristics were specific to a subset of lipid species and, as such, likely a regulated process downstream of *CDKN2A*. In agreement with this idea, we found that shRNA-mediated silencing of p14/p16 expression in *CDKN2A* WT GSs shifted the composition and acyl tail characteristics of differentially abundant lipid species toward that of *CDKN2A*-deleted GSs (Figures 2G, S4A, and S4B). Intriguingly, however, the link between *CDKN2A* deletion and altered lipid composition found in GSs could not be detected from a prior lipidomic analysis of established glioma cell lines (Figure S4C),[6] emphasizing the value and importance of utilizing primary samples. Together, these data suggest that *CDKN2A* status has a profound effect on the tail length and saturation state of a subset of lipids in GBM.

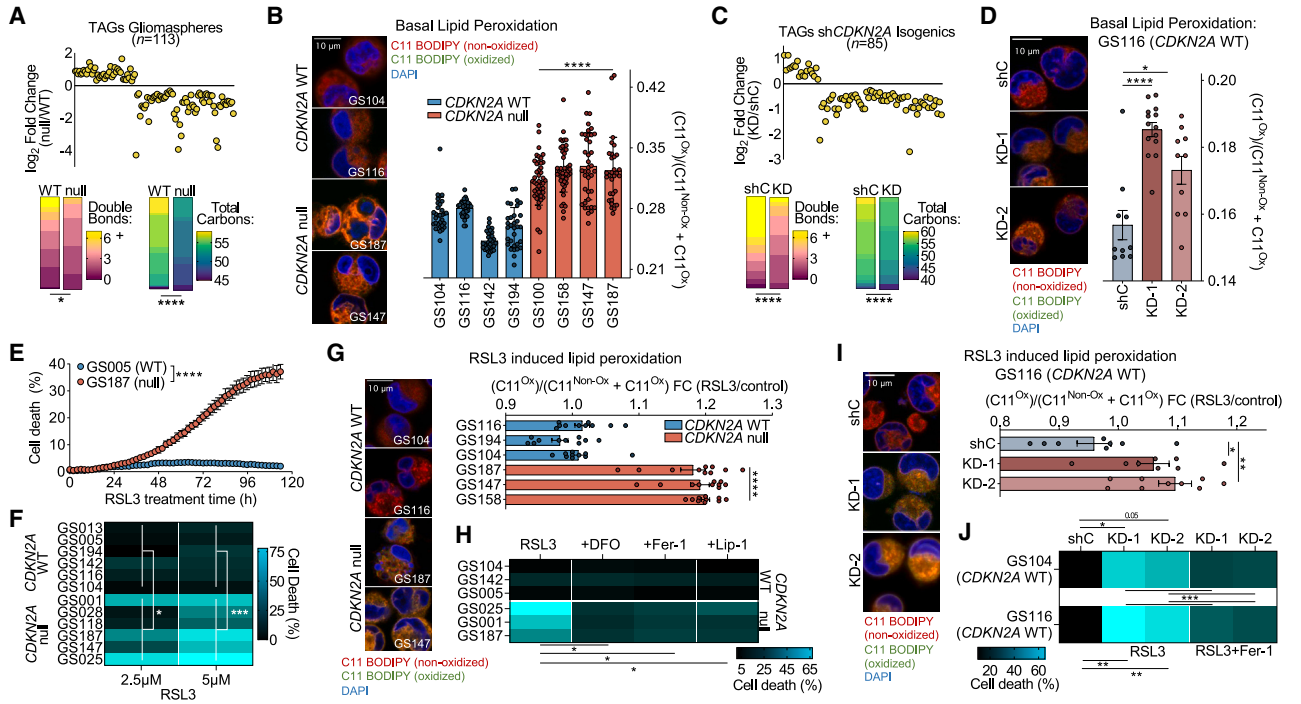

Figure 3. *CDKN2A* deletion renders GBM susceptible to ferroptosis

(A) Log_2 fold change of significantly different (Student's t test p value < 0.05) TAG species in *CDKN2A* null/WT GSs, ordered by directionality of change, total tail length, and total double bond number. Stacked bar chart indicates double bond and total carbon composition (Student's two-sample t test).

(B) Confocal microscopy images showing basal C11-BODIPY 581/591 lipid peroxidation in *CDKN2A* WT and *CDKN2A* null GSs. Scale bar represents 10 μm (60x magnification). Quantification of basal C11-BODIPY lipid peroxidation across *CDKN2A* WT and *CDKN2A* null GSs is plotted as a bar chart. Each point represents an individual cell. Mean ± SD (Student's two-sample t test).

(C) Log_2 fold change of significantly different TAG species with sh*CDKN2A* (Student's t test p value < 0.05) ordered by directionality of change, total tail length, and total double bond number. Stacked bar chart indicates double bond and total carbon composition (Student's two-sample t test).

(D) Quantification of basal C11-BODIPY lipid peroxidation in GS116 (*CDKN2A* WT) infected with shC, KD-1, or KD-2. See (B).

(E) Representative trace of cell death (%) under 2.5 μM RSL3 treatment over time (h) from the Incucyte live cell imaging system in a *CDKN2A* WT and null GS (two-way ANOVA followed by Tukey's post-hoc test).

(F) Heatmap of cell death (%) after 72 h of treatment with RSL3 (2.5 μM and 5 μM) in *CDKN2A* WT and *CDKN2A* null GSs (significance calculated by Student's two-sample t test).

(G) Confocal microscopy images showing C11-BODIPY peroxidation induced after 24h treatment with 2.5 μM RSL3 in *CDKN2A* WT and *CDKN2A* null GSs. Quantification of C11-BODIPY peroxidation is plotted as fold change of RSL3 treatment/DMSO control. Each point represents an individual cell. Mean ± SD (Student's two-sample t test). FC, fold-change.

(H) Heatmap of cell death (%) after 72 h of treatment with 2.5 μM RSL3 with or without the addition of canonical ferroptosis inhibitors (100 μM DFO, 1 μM ferrostatin-1, or 1 μM liproxstain-1) in *CDKN2A* WT and null GSs (Student's two-sample t test).

(I) Confocal microscopy images showing C11-BODIPY peroxidation with DMSO control treatment or 2.5 μM RSL3 treatment after 24 h in GS116 infected with shC, KD-1, or KD-2. See (G).

(J) Heatmap of cell death (%) after 72 h of treatment with 2.5 μM RSL3 treatment with and without the addition 1 μM ferrostatin-1 in GS104 or GS116 infected with shC, KD-1, or KD-2 (Student's two-sample t test). p > 0.05 = ns; p < 0.05 = *; p < 0.01 = **; p < 0.001 = ***; p < 0.0001 = ****. See also Figure S5.

Consistent with the diverse impact on lipid composition observed in *CDKN2A* null GBM, RNA sequencing (RNA-seq) analysis of our GSs revealed changes in the expression level of several lipid metabolic genes associated with *CDKN2A* deletion (Figure S4D). Transcripts representing all lipid gene clusters distinguished *CDKN2A* WT from *CDKN2A* null GBM, with over 160 genes associated with the synthesis of various lipid classes and modifications to acyl tails differentially expressed between the genotypes (Figure S4E). Moreover, the patterns of gene cluster enrichments observed between our *CDKN2A* WT and null GBM samples were preserved in RNA-seq data of GBM tumors obtained from The Cancer Genome Atlas (TCGA) dataset (n = 139 samples with available RNA-seq and somatic alteration profiling) (Figure S4F). Thus, the considerable shifts in lipid composition with *CDKN2A* deletion are associated with significant changes in lipid gene expression programs.

CDKN2A deletion sensitizes GBM cells to lipid peroxidation and ferroptosis

CDKN2A deletion affects composition across all lipid subclasses; however, triacylglycerides were the majority (58%) of the individual lipid species altered in *CDKN2A* null GSs (Figure 3A). While there were no differences in total TAG levels (Figure S5A), further examination revealed that the fraction of longer chain, highly desaturated TAGs was significantly reduced in *CDKN2A*-deleted GSs. Conversely, shorter chain saturated fatty

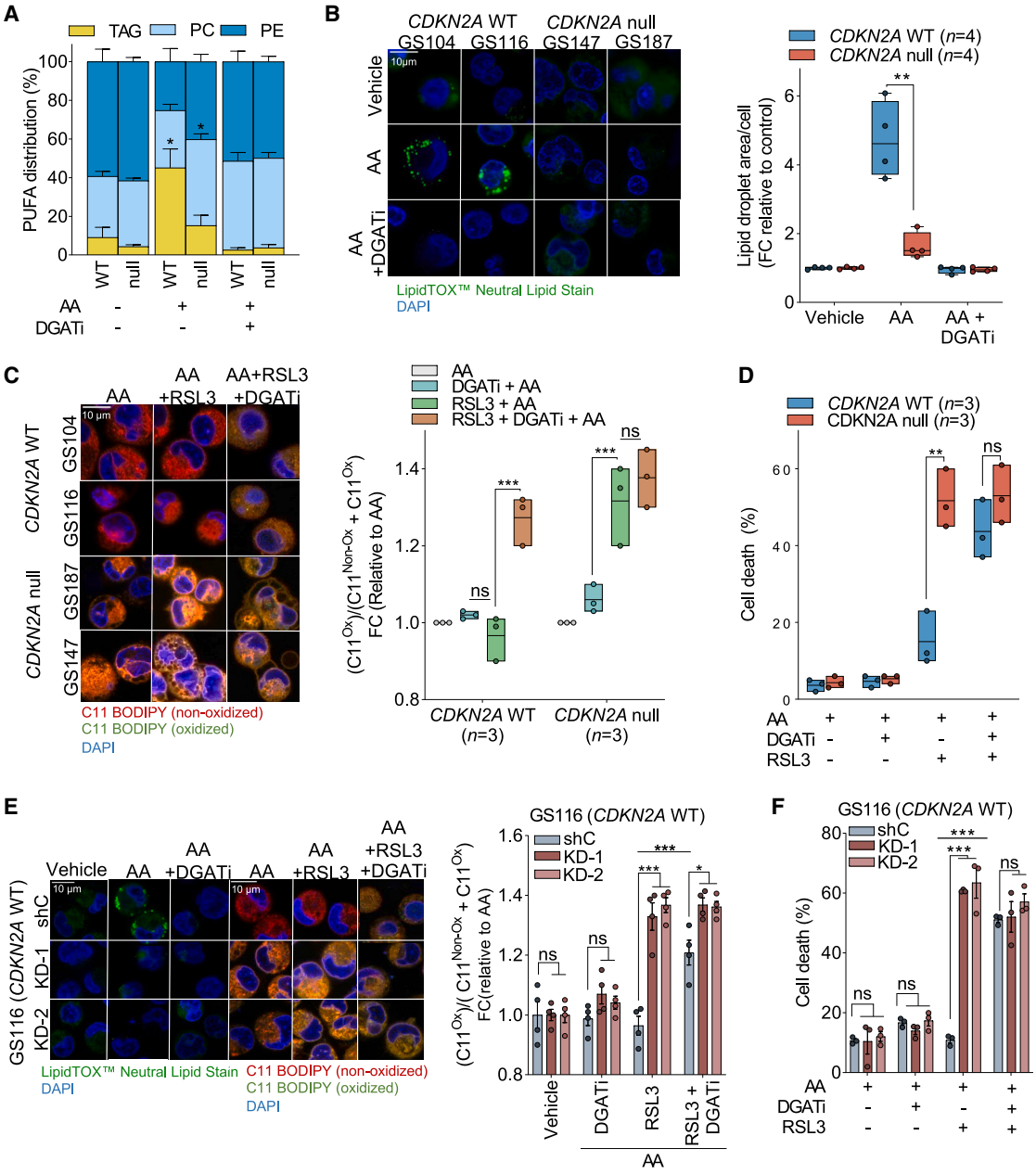

Figure 4. PUFA TAGs are protective against lipid peroxidation and ferroptosis in *CDKN2A* WT GBM

(A) Stacked bar chart showing PUFA distribution (% of total) within TAGs, PCs, and PEs in *CDKN2A* WT (n = 3) and null (n = 3) GSs under basal (AA–, DGATi–) conditions or with 24 h 75 μM arachidonic acid (AA) treatment with or without co-treatment with 20 μM DGAT1 and 10 μM DGAT2 inhibitors (DGATi). Mean ± SEM (Student's two-sample t test).

(B) Confocal microscopy images showing accumulation of the LipidTOX neutral lipid stain in *CDKN2A* null and WT GSs treated with DMSO Vehicle (DMSO), 75 μM AA, or 75 μM AA + 20 μM DGAT1 inhibitor + 10 μM DGAT2 inhibitor for 24 h. Scale bar represents 10 μm (60x magnification). Quantification of lipid droplet area per cell across *CDKN2A* WT (n = 4) and null (n = 4) GSs across these same conditions relative to its respective DMSO control is shown. Each dot represents the average quantification per cell line for the specified condition. Mean ± SD (Student's two-sample t test).

(C) Confocal images showing C11-BODIPY peroxidation induced after 24 h treatment with 75 μM AA, 75 μM AA + 2.5 μM RSL3, or 75 μM AA + 2.5 μM RSL3 + 20 μM DGAT1 inhibitor +10 μM DGAT2 inhibitor in *CDKN2A* null and WT GSs. Quantification of C11-BODIPY peroxidation is plotted as fold change relative to 24 h of 75 μM AA treatment. Each dot represents the average quantification per cell line. Mean ± SD (Student's two-sample t test).

(D) Cell death (%) after 72 h of treatment with the same conditions shown in Figure 4C in *CDKN2A* WT (n = 3) and null (n = 3) GS. Each dot represents the average cell death per cell line for the specified condition. Mean ± SD (Student's two-sample t test).

(E) Confocal images showing accumulation of the LipidTOX neutral lipid stain with 24 h of the same treatments indicated in (B) and C11-BODIPY peroxidation with 24 h treatment of the same conditions indicated in (C) in GS116 (*CDKN2A* WT) infected with shC, KD-1, or KD-2. Quantification of C11-BODIPY peroxidation is

(legend continued on next page)

acid (SFA)-containing and monounsaturated fatty acid (MUFA)-containing TAGs were enriched in *CDKN2A*-deleted cells relative to *CDKN2A* WT counterparts (Figure 3A). Membrane phospholipids (e.g., phosphatidylethanolamines [PEs] and phosphatidylcholines [PCs]) containing long acyl chain PUFAs are highly sensitive to lipid peroxidation, especially compared with phospholipid species with SFAs or MUFAs.[28] By contrast, PUFAs localized in TAGs are sequestered within lipid droplets where they are protected against lipid oxidation.[29] We hypothesized that the reduced abundance of long chain PUFA TAGs in *CDKN2A* null GBM tumors would increase lipid peroxidation. Consistent with this hypothesis, we observed greater basal lipid peroxidation, using the lipid oxidation probe C11 BODIPY 581/591, in *CDKN2A* null cells, when compared with their *CDKN2A* WT counterparts (Figures 3B and S5B). Likewise, silencing of p14/p16 expression in *CDKN2A* WT GSs decreased PUFA TAGs containing longer acyl chain tails (Figure 3C), with an increase in lipid peroxidation relative to non-silenced control cells (Figure 3D). Thus, we conclude that *CDKN2A* deletion shifts the acyl tail characteristics of the TAG pool resulting in high basal levels of lipid peroxidation in GBM.

Ferroptosis is a non-apoptotic cell death mechanism defined by a dependence on iron and by the lethal accumulation of lipid peroxides.[30] Having found that *CDKN2A* deletion is associated with increased basal lipid peroxidation, we posited that *CDKN2A* null GSs would be sensitized to induction of ferroptosis. Across a panel of *CDKN2A* null GSs (n = 6), inhibition of glutathione peroxidase 4 (GPX4) with (1*S*,3*R*)-RSL3 (RSL3) or ML210[31] resulted in pronounced cell death. Conversely, *CDKN2A* WT GSs (n = 6) were largely insensitive to both compounds (Figures 3E, 3F, and S5C). Consistent with the greater susceptibility of *CDKN2A* null GBMs to lethal lipid peroxidation, GPX4 inhibition increased lipid peroxidation only in *CDKN2A* null GSs and not in *CDKN2A* WT cells (Figure 3G). RSL3- or ML210-induced cell death was suppressed by the ferroptosis inhibitors ferrostatin-1 (Fer-1), liproxstatin-1 (Lip-1), the iron chelator deferoxamine (DFO), or by treatment with deuterated linolenic acid, which is far less sensitive to peroxidation than normal PUFAs (Figures 3H and S5D–S5F).[32–34] Moreover, *CDKN2A* null GSs were more sensitive than their WT counterparts to erastin-2, an inducer of ferroptosis via its ability to inhibit the cystine-glutamate antiporter xCT (Figure S5G). Finally, silencing of p14/p16 in *CDKN2A* WT GSs increased lipid peroxidation and ferroptosis susceptibility (Figures 3I and 3J). Thus, disruption of *CDKN2A*, and specifically loss of p14/16 expression, renders GBM more susceptible to lipid peroxidation and ferroptosis.

CDKN2A deletion reduces oxidizable PUFA sequestration into lipid droplets

We sought to better understand how *CDKN2A* deletion selectively sensitizes GBM cells to ferroptosis. As noted, peroxidation of PUFA-containing phospholipids contributes to the execution of ferroptosis,[35] and sequestration of PUFAs into the TAG pool has been suggested to limit ferroptosis.[36] Therefore, we posited that *CDKN2A* governs the partitioning of oxidizable PUFAs into the TAG pool, consequently modulating sensitivity to lipid peroxidation and ferroptosis. To begin testing this hypothesis, we provided the PUFA arachidonic acid (AA) to *CDKN2A* WT (n = 3) and null (n = 3) GSs and performed lipidomics; AA treatment significantly increased the sequestration of PUFAs into TAG species in *CDKN2A* WT GSs. By contrast, AA addition to *CDKN2A* null cells specifically expanded the AA-containing PC phospholipid pools (Figure 4A). Moreover, AA treatment markedly increased lipid droplet formation in *CDKN2A* WT GSs but not in *CDKN2A* null counterparts (Figure 4B). Both the expanded PUFA TAG pool and the increase in lipid droplets observed with AA addition to *CDKN2A* WT GBM cells were blocked by pharmacologic inhibition of DGAT1 and DGAT2, which are key enzymes in TAG biosynthesis (Figures 4A and 4B).[37] Finally, we saw no differences in the relative abundance of cellular SFAs and MUFAs (e.g., 16:0, 16:1, 18:0, and 18:1) between *CDKN2A* WT and *CDKN2A* null GSs, consistent with the genotypes having similar *de novo* fatty acid synthetic capability (Figure S6A).

Our results demonstrate that *CDKN2A* genetic status impacts intracellular PUFA distribution into distinct lipids classes (e.g., TAGs and phospholipids). Moreover, these *CDKN2A*-mediated changes in lipid composition underlie susceptibility of GBM to lipid peroxidation and ferroptosis. In agreement with this idea, providing exogenous AA markedly increased RSL3-mediated lipid peroxidation and ferroptosis in *CDKN2A* null GBM cells. In distinction, DGAT1/2 inhibitors were required for AA-treated *CDKN2A* WT cells to increase RSL3-induced lipid peroxidation and ferroptosis to the levels observed in *CDKN2A* null GSs (Figures 4C, 4D, and S6B). Taken together, these data support a model in which p14/16 signaling regulates the shunting of PUFAs into the TAG compartment, resulting in protection from lipid peroxidation and ferroptosis in GBM.

Loss of p16 is sufficient to render GBM sensitive to ferroptosis

CDKN2A encodes two proteins, p14 and p16. Canonically, p14 dictates cell fate by indirectly stabilizing p53, while p16 suppresses tumor formation by inhibiting CDK4/6.[25,26] While a direct role for p14 or p16 in regulating cancer lipid metabolism has not been described, recent findings show that p16 contributes to hepatic lipid homeostasis.[38] These observations led us to posit that p16 may regulate GBM lipid metabolism and consequent sensitivity to ferroptosis. To test this hypothesis, we first ablated *CDKN2A* using CRISPR-Cas9 in *CDKN2A* WT GSs using sgRNAs targeting exon 2 of *CDKN2A* (shared between p14 and p16) (Figures S7A and S7B).[39] Knockout of exon 2 of *CDKN2A* (*CDKN2A* ex2 KO) abrogated p14 and p16 protein levels and, similar to our findings in *CDKN2A* null GSs, reduced the enrichment for desaturated long chain acyl tail lipid species (Figure S7C), with a notable decrease in the fraction of PUFA-containing TAGs (Figure 5A).

plotted as fold change relative to 24 h of 75 μM AA treatment. Each point represents the average quantification per image for the specified condition and cell line. Mean ± SD (Student's two-sample t test).

(F) Cell death (%) after 72 h of the same treatment indicated in (D) in GS116 (*CDKN2A* WT) infected with shC, KD-1, or KD-2. Each point represents a biological replicate. Mean ± SD (significance calculated by Student's two-sample t test). $p > 0.05$ = ns; $p < 0.05$ = *; $p < 0.01$ = **; $p < 0.001$ = ***; $p < 0.0001$ = ****. See also Figure S6.

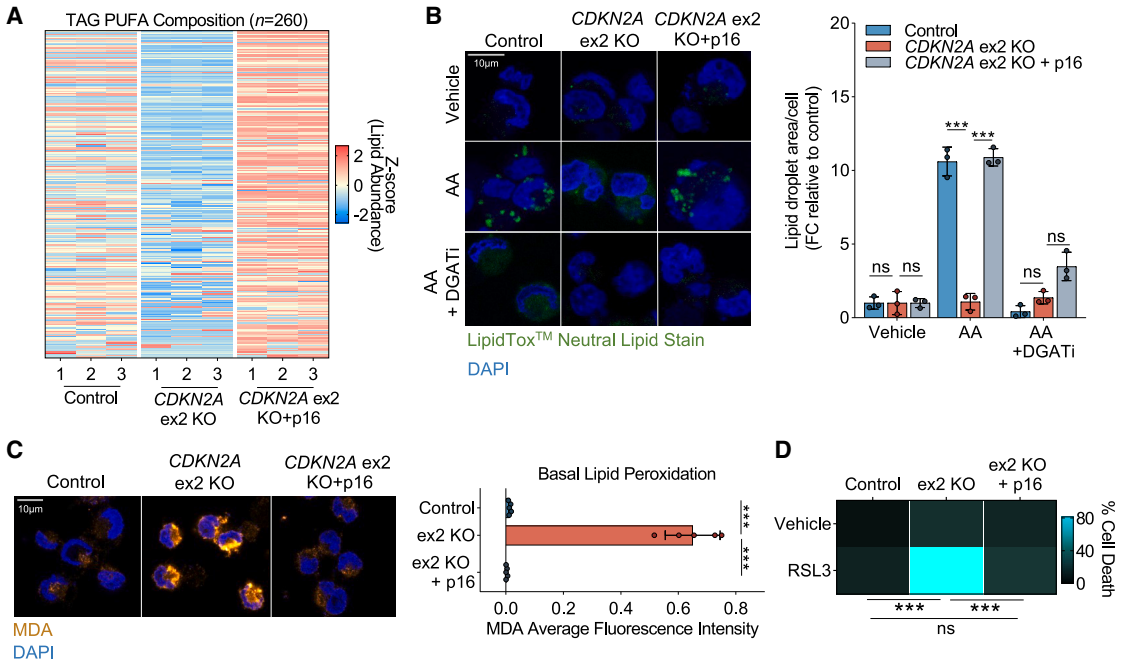

Figure 5. Loss of p16 is sufficient to sensitize GBM to ferroptosis

(A) Abundance of PUFA TAGs (n = 260 lipid species, species % of class) between GS116 (*CDKN2A* WT) transfected with control, *CDKN2A* ex2 KO, or *CDKN2A* ex2 KO + p16 addback. Z-scores are across GS116 control, *CDKN2A* ex2 KO, and *CDKN2A* ex2 KO + p16.

(B) Confocal microscopy images showing accumulation of the LipidTOX neutral lipid stain in GS116 control, *CDKN2A* ex2 KO, or *CDKN2A* ex2 KO + p16 addback. Cells were treated with Vehicle (DMSO), 75 μM AA, or 75 μM AA + 20 μM DGAT1 inhibitor +10 μM DGAT2 inhibitor for 24 h. Scale bar represents 10 μm (60x magnification). Quantification of lipid droplet area/cell (fold change relative to control) is shown. Each dot represents the average quantification per cell line for the specified condition. Mean ± SD (Student's two-sample t test).

(C) Confocal images showing basal malondialdehyde (MDA) immunofluorescence staining. Quantification of MDA average fluorescent intensity/cell is plotted. Each dot represents the average intensity per cell line. Mean ± SD (significance calculated with parametric unpaired t test).

(D) Heatmap of cell death (%) induced by DMSO vehicle or 2.5 μM RSL3 after 72 h of treatment (Student's two-sample t test). $p > 0.05$ = ns; $p < 0.05$ = *; $p < 0.01$ = **; $p < 0.001$ = ***; $p < 0.0001$ = ****. See also Figure S7.

Next, we reintroduced p16 into our *CDKN2A* ex2 KO cells to specifically restore p16 protein levels while maintaining reduced p14 expression (Figures S7A and S7B). p16 addback rescued many of the lipidomic features to that of *CDKN2A* WT control GSs, including enriched lipid species with very long chain and desaturated acyl tails (Figure S7C) and an increase in PUFA TAGs (Figure 5A). The rescue of PUFA TAG levels with p16 addback was coupled with a restored ability to shunt AA into lipid droplets (Figure 5B). These data further support a model where *CDKN2A* partitions oxidizable PUFA TAGs in lipid droplets. Correspondingly, we observed that addback of p16 expression could completely reverse basal lipid peroxidation levels, as determined by measuring both the lipid peroxidation by-product malondialdehyde (MDA) (Figure 5C) and ferroptosis sensitivity relative to *CDKN2A* ex2 KO cells (Figure 5D). These results led us to conclude that p16 loss is sufficient to remodel components of the GBM lipidome, rendering GBM GSs susceptible to ferroptosis.

GPX4 inhibition decreases *CDKN2A*-deleted GBM tumor burden *in vivo*

We next explored whether *CDKN2A* genetic status influences the lipidome and ferroptotic potential of GBM tumors *in vivo*. In agreement with our cell culture findings, *CDKN2A* WT orthotopic PDX tumors (n = 11) were enriched with TAGs containing longer acyl tails and more double bonds relative to *CDKN2A* null tumors (n = 18) (Figure 6A). *CDKN2A* null PDX tumors also displayed higher levels of lipid peroxidation when compared with *CDKN2A* WT PDX tumors (Figures 6B and S8A). This result suggests that the *CDKN2A* null tumors would be more sensitive to the induction of ferroptosis. To test this hypothesis, we disrupted *GPX4* expression using CRISPR-Cas9 in *CDKN2A* WT (n = 2) and *CDKN2A* null (n = 2) GSs (Figure 6C). As anticipated, genetic *GPX4* ablation resulted in significantly higher ferroptosis in *CDKN2A* null GSs compared with WT GSs *in vitro* (Figures S8B–S8D). Next, we engineered a separate cohort of *CDKN2A* WT and *CDKN2A* null GSs with either non-targeting control (NT) sgRNAs or three different *GPX4* sgRNAs. Transduced GSs were expanded in medium containing Fer-1 (to prevent changes in viability with *GPX4* ablation) for 72 h and then implanted into the brains of NOD-scid gamma (NSG) mice. All three *GPX4* sgRNAs significantly extended the survival of two different *CDKN2A* null PDX models (PDX025 and PDX187) relative to animals implanted with cells transduced with NT sgRNAs (Figure 6D). By contrast, disruption of *GPX4* had no survival benefit for mice bearing *CDKN2A* WT PDX tumors (PDX005 and PDX208) (Figure 6D). Together, these results demonstrate that GPX4 inhibition significantly and selectively improves the outcomes of mice bearing *CDKN2A* null GBM tumors.

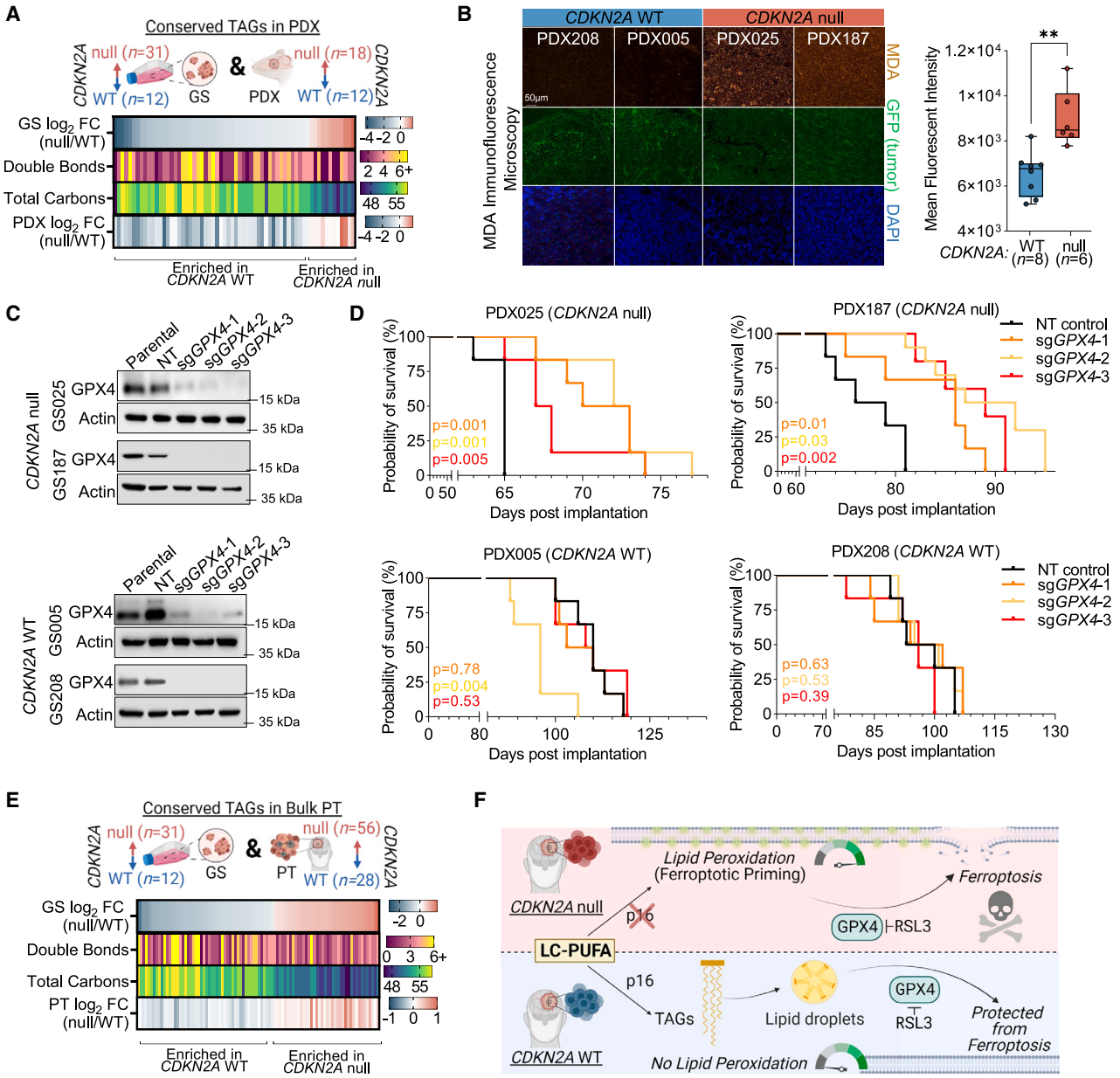

Figure 6. *CDKN2A* deletion induces lipid peroxidation and susceptibility to ferroptosis in GBM orthotopic xenografts

(A) Heatmap showing enrichment of conserved TAGs between GSs and PDXs. TAGs enriched in *CDKN2A* WT tumors have a $\log^2$ fold change (null/WT) < 0 (blue), while TAGs enriched in *CDKN2A* null tumors have a $\log_2$ fold change (null/WT) > 0 (pink). Total double bonds and total carbon length are annotated within heatmap.

(B) Immunofluorescence microscopy of *CDKN2A* WT and *CDKN2A* null tumors stained for MDA (orange), GFP (GFP tumor) (green), and DAPI (blue). Scale bar represents 50 μm (20x magnification). Quantification of MDA (mean fluorescent intensity) across *CDKN2A* WT (n = 8) and null (n = 6) PDX tissue. Boxplots show mean (middle line) +/− SD. Whiskers represent minimum and maximum data points (significance calculated by Mann-Whitney t test).

(C) Western blot of GPX4 and actin in CDKN2A null gliomaspheres (GS025, GS187) and WT (GS005, GS208) infected with nothing (parental), CRISPR non-targeting control (NT), or sgRNAs targeting *GPX4* (sg*GPX4*-1, sg*GPX4*-2, sg*GPX4*-3). Molecular weight of closest ladder marker is indicated to the right.

(D) Kaplan-Meier plot showing probability of survival (%) in mice harboring *CDKN2A* null and WT orthotopic tumors infected with NT (n = 6), sg*GPX4*-1 (n = 6), sg*GPX4*-2 (n = 6 for PDX025, PDX005, PDX208, n = 10 for PDX187), or sg*GPX4*-3 (n = 6). X-axis indicates days post tumor implantation. Significance was calculated with log rank (Mantel-Cox) test between the survival curves for NT vs. individual guides.

(E) Heatmap showing enrichment of conserved TAGs between GSs and tumors from patients with GBM (PT). TAGs enriched in *CDKN2A* WT tumors have a $\log_2$ fold change (null/WT) < 0 (blue), while TAGs enriched in *CDKN2A* null tumors have a $\log_2$ fold change (null/WT) > 0 (pink).

(F) Proposed mechanism of ferroptotic sensitivity in *CDKN2A* WT and *CDKN2A* null GBM. p > 0.05 = ns; p < 0.05 = *; p < 0.01 = **; p < 0.001 = ***; p < 0.0001 = ****. See also Figure S8.

Finally, we asked whether the specific PUFA TAG lipid phenotype linked with *CDKN2A* genetic status was conserved in tumors from patients with GBM. Like our preclinical GBM models, *CDKN2A* deletion in GBM tumors (n = 50) was associated with reduced fraction of TAGs containing highly desaturated long acyl tails relative to *CDKN2A* WT tumors (n = 34) (Figure 6E). These data emphasize the clinical relevance of our cell culture and xenograft findings and further support the conclusion that lipid metabolic remodeling due to loss of *CDKN2A* increases membrane lipid peroxidation and consequently primes GBM for ferroptosis (Figure 6F).

DISCUSSION

The influences of molecular heterogeneity and environment on the metabolic features of cancer cells can confound our ability to identify translatable metabolic vulnerabilities that are exploitable in therapy.[7,10,11] Here, we created a resource containing both molecular and lipidomic data from GBM tumor samples, together with derivative *in vitro* and *in vivo* models. This dataset will enable investigations into the genetic influences on GBM lipid metabolism and potential impacts of the tumor environment. We demonstrate the utility of this resource by integrating molecular and lipidomic features of our GBM sample cohort to discover that deletion of a recurring tumor suppressor, *CDKN2A*, remodels the GBM lipidome. Crucially, GBM lipid composition is similarly remodeled with *CDKN2A* deletion in the human brain, as a xenograft in the mouse brain, and when grown as GSs in cell culture. This concordance across environments (*in vitro* and *in vivo*) increases the translational potential of this metabolic vulnerability in patients with GBM having *CDKN2A* deletion. We anticipate and encourage others to use this dataset to uncover other potential therapeutically actionable approaches for this deadly disease.

How *CDKN2A* regulates the GBM lipidome remains less clear. Our gene expression data indicate large changes in lipid metabolic programming with deletion of *CDKN2A* in GBM, and we posit it unlikely that the molecular underpinning of how *CDKN2A* influences the lipidome can be attributed to a single lipid metabolic gene or pathway. Moreover, there is tight substrate and feedback regulation of lipid enzymes, so the lipidome of *CDKN2A* null GBM likely represents a composite of transcriptional and post-translation regulation. Our data show that p16 encoded by *CDKN2A* acts as a fundamental regulator of lipid composition and protection from ferroptotic priming in GBM through its ability to alter acyl tail composition and shunting of fatty acids into TAGs within lipid droplets. Interestingly, *CDKN2A* has been previously linked to metabolic syndrome, to hepatic fatty acid oxidation, and to ketogenesis, as well as to adipose tissue differentiation.[38,40,41] Although the molecular mechanisms linking *CDKN2A* with lipid metabolism in normal tissues are also not well understood, these observations, combined with our studies, suggest a fundamental role for *CDKN2A* in regulating cellular lipid composition in normal and neoplastic tissues. Undoubtedly, deep mechanistic work deconvoluting how a cell cycle regulatory protein influences lipid composition of normal and malignant cells will be an important goal of future studies. Finally, as the expression of several other genes adjacent to *CDKN2A* are similarly downregulated with deletion of this locus, including those encoding metabolic enzymes (e.g., MTAP, HACD4), we cannot exclude the possibility that their loss also contributes to altered GBM lipid metabolism in *CDKN2A*-deleted GBMs.

The ferroptosis pathway is emerging as a candidate therapeutic target in several cancers.[42,43] We find that loss of *CDKN2A* primes a large subset of patient-derived GBM models to ferroptosis both *in vitro* and in orthotopic xenografts. One important concept in ferroptosis is that sequestration of oxidizable PUFAs into specific lipid species or subcellular compartments can buffer susceptibility to oxidative stress and induction of cell death.[29,36] Supporting this mechanism, our data demonstrate that the sensitivity of *CDNK2A* null GBM to ferroptosis is associated with differences in the partitioning of oxidizable PUFAs into TAGs and lipid droplets. Our results provide proof-of-concept evidence that GPX4 may be a relevant therapeutic target for a large, genetically stratified subset of patients with GBM. There are currently no pharmacological GPX4 inhibitors suitable for use in the brain; our findings provide a strong rationale for developing brain-penetrant small molecules that induce lipid peroxidation-mediated GBM cell death via inhibition of GPX4 or other ferroptotic targets. In summary, our study provides a framework for the combined use of preclinical and clinical tumor samples to investigate the impact of molecular diversity on metabolic heterogeneity, with the goal of identifying clinically relevant metabolic vulnerabilities.

STAR★METHODS

Detailed methods are provided in the online version of this paper and include the following:

- KEY RESOURCES TABLE
- RESOURCE AVAILABILITY
  - Lead contact
  - Materials availability
  - Data and code availability
- EXPERIMENTAL MODEL AND SUBJECT DETAILS
  - Patient-derived GBM tumors and gliomaspheres
  - Mice
  - Patient-derived orthotopic xenografts
- METHOD DETAILS
  - Secreted *Gaussia* luciferase measurements
  - Genetic manipulations
  - Immunoblotting
  - Exogenous fatty acid addition – shotgun lipidomics
  - Shotgun lipidomics
  - Annotating lipid species characteristics
  - Fatty acid analysis
  - Quantifying lipid peroxidation with BODIPY 581/591 C11
  - Cell death kinetics – Incucyte
  - Cell death kinetics – Trypan blue exclusion
  - Quantifying MDA levels with immunofluorescent microscopy - Tissue
  - Quantifying MDA levels with immunofluorescent microscopy - Cells
  - Lipid droplet imaging and quantification
  - Whole exome and RNA sequencing
  - Whole exome QC and mapping
  - RNA-seq QC and mapping

- Somatic mutation and copy number alteration calling
- Integrated *CDKN2A* status based on whole exome and RNA sequencing
- Lipidome-transcriptome correlation analysis
- Correlation cluster annotation and lipid-gene cluster co-enrichment
- Genetic alteration - lipid cluster enrichment scoring
- Gene cluster scoring and genomic association testing
- Differential expression analysis
- Principal component analysis and varimax rotation
- Differential lipid abundance permutation analysis
- TCGA GBM multi-omics data and analysis
- Gene expression subtyping

● QUANTIFICATION AND STATISTICAL ANALYSIS

SUPPLEMENTAL INFORMATION

Supplemental information can be found online at https://doi.org/10.1016/j.ccell.2023.05.001.

ACKNOWLEDGMENTS

The authors thank Dr. Harvey Herschman, Dimitri Cadet, Dr. Jonathan Tsang, and other past and present members of the Nathanson lab for their valuable critiques and discussions. We thank Dr. Mikhail Shchepiniov for deuterated PUFAs. We further acknowledge Dr. Michaela Veliova for feedback regarding experimental planning. We thank the Brain Tumor Translational Resource (BTTR) and Dr. Xinmin Li with the Center for Genomics and Bioinformatics (TCGB) for recruitment of tumor specimens and sequencing, respectively. All graphics created with Biorender (Biorender.com). Finally, we are grateful to the patients with brain cancer and their families who consented to donating tumor tissue for this research. This work was funded by NIH grants R01NS121319 (D.A.N., S.J.B., S.J.D.), P50CA211015 (D.A.N., T.F.C., S.J.B., T.G.G., L.M.L.), P50CA211015 (D.A.N., T.F.C., S.J.B., T.G.G., L.M.L.), R01CA227089 (D.A.N., T.G.G., T.F.C., L.M.L.), P01HL146358 (S.J.B.), and the Department of Defense grant W81XWH-20-1-0453 (J.K.M., D.M., D.A.N.).

AUTHOR CONTRIBUTIONS

Conceptualization: D.M., K.J.W., S.J.D., S.J.B., and D.A.N. Methodology: J.K.M., N.A.B., D.M., S.B., A.J., A.S., T.G.G., K.J.W., S.J.D., S.J.B., and D.A.N. Investigation: D.M., J.K.M., J.J.S., E.G.F., N.A.B., H.Z., and C.T. Visualization: D.M., J.K.M., N.A.B., J.J.S., E.G.F., C.T., R.P., T.G.G., K.J.W., S.J.D., S.J.B., and D.A.N. Funding acquisition: D.A.N., S.J.B., S.J.D., T.G.G., and L.M.L. Project administration: D.A.N. Supervision: D.A.N., S.J.D., S.J.B., and T.G.G. Clinical specimens: T.F.C. and L.M.L. Writing – original draft: J.K.M., D.M., N.A.B., and D.A.N. Writing – review & editing: E.G.F., J.J.S., T.G.G., K.J.W., S.J.D., and S.J.B.

DECLARATION OF INTERESTS

D.A.N. is a co-founder of Trethera Corporation and has equity in the company. D.A.N. and T.F.C. are co-founders of Katmai Pharmaceuticals and have equity in the company. S.J.D. is co-founder of Prothegen, Inc., serves on the scientific advisory board of and Hillstream BioPharma, and holds patents related to ferroptosis. T.G.G. has consulting and equity agreements with Auron Therapeutics, Boundless Bio, Coherus BioSciences, and Trethera Corporation.

INCLUSION AND DIVERSITY

We support inclusive, diverse, and equitable conduct of research.

Received: September 20, 2022
Revised: February 27, 2023
Accepted: May 2, 2023
Published: May 25, 2023

REFERENCES

1. Ying, H., Kimmelman, A.C., Lyssiotis, C.A., Hua, S., Chu, G.C., Fletcher-Sananikone, E., Locasale, J.W., Son, J., Zhang, H., Coloff, J.L., et al. (2012). Oncogenic Kras maintains pancreatic tumors through regulation of anabolic glucose metabolism. Cell *149*, 656–670. https://doi.org/10.1016/J.CELL.2012.01.058.
2. Garcia-Cao, I., Song, M.S., Hobbs, R.M., Laurent, G., Giorgi, C., De Boer, V.C.J., Anastasiou, D., Ito, K., Sasaki, A.T., Rameh, L., et al. (2012). Systemic elevation of PTEN induces a tumor-suppressive metabolic state. Cell *149*, 49–62. https://doi.org/10.1016/J.CELL.2012.02.030.
3. Dang, L., White, D.W., Gross, S., Bennett, B.D., Bittinger, M.A., Driggers, E.M., Fantin, V.R., Jang, H.G., Jin, S., Keenan, M.C., et al. (2009). Cancer-associated IDH1 mutations produce 2-hydroxyglutarate. Nature *462*, 739–744. https://doi.org/10.1038/nature08617.
4. Maddocks, O.D.K., Berkers, C.R., Mason, S.M., Zheng, L., Blyth, K., Gottlieb, E., and Vousden, K.H. (2012). Serine starvation induces stress and p53-dependent metabolic remodelling in cancer cells. Nature *493*, 542–546. https://doi.org/10.1038/nature11743.
5. Kim, J., Lee, H.M., Cai, F., Ko, B., Yang, C., Lieu, E.L., Muhammad, N., Rhyne, S., Li, K., Haloul, M., et al. (2020). The hexosamine biosynthesis pathway is a targetable liability in KRAS/LKB1 mutant lung cancer. Nat. Metab. *2*, 1401–1412. https://doi.org/10.1038/s42255-020-00316-0.
6. Li, H., Ning, S., Ghandi, M., Kryukov, G.V., Gopal, S., Deik, A., Souza, A., Pierce, K., Keskula, P., Hernandez, D., et al. (2019). The landscape of cancer cell line metabolism. Nat. Med. *25*, 850–860. https://doi.org/10.1038/s41591-019-0404-8.
7. Chen, P.H., Cai, L., Huffman, K., Yang, C., Kim, J., Faubert, B., Boroughs, L., Ko, B., Sudderth, J., McMillan, E.A., et al. (2019). Metabolic diversity in human non-small cell lung cancer cells. Mol. Cell *76*, 838–851.e5. https://doi.org/10.1016/J.MOLCEL.2019.08.028.
8. Domcke, S., Sinha, R., Levine, D.A., Sander, C., and Schultz, N. (2013). Evaluating cell lines as tumour models by comparison of genomic profiles. Nat. Commun. *4*, 1–10. https://doi.org/10.1038/ncomms3126.
9. Lee, J., Kotliarova, S., Kotliarov, Y., Li, A., Su, Q., Donin, N.M., Pastorino, S., Purow, B.W., Christopher, N., Zhang, W., et al. (2006). Tumor stem cells derived from glioblastomas cultured in bFGF and EGF more closely mirror the phenotype and genotype of primary tumors than do serum-cultured cell lines. Cancer Cell *9*, 391–403. https://doi.org/10.1016/J.CCR.2006.03.030.
10. Marin-Valencia, I., Yang, C., Mashimo, T., Cho, S., Baek, H., Yang, X.L., Rajagopalan, K.N., Maddie, M., Vemireddy, V., Zhao, Z., et al. (2012). Analysis of tumor metabolism reveals mitochondrial glucose oxidation in genetically diverse human glioblastomas in the mouse brain in vivo. Cell Metab. *15*, 827–837. https://doi.org/10.1016/J.CMET.2012.05.001.
11. Davidson, S.M., Papagiannakopoulos, T., Olenchock, B.A., Heyman, J.E., Keibler, M.A., Luengo, A., Bauer, M.R., Jha, A.K., O'Brien, J.P., Pierce, K.A., et al. (2016). Environment impacts the metabolic dependencies of ras-driven non-small cell lung cancer. Cell Metab. *23*, 517–528. https://doi.org/10.1016/J.CMET.2016.01.007.
12. Barekatain, Y., Ackroyd, J.J., Yan, V.C., Khadka, S., Wang, L., Chen, K.C., Poral, A.H., Tran, T., Georgiou, D.K., Arthur, K., et al. (2021). Homozygous MTAP deletion in primary human glioblastoma is not associated with elevation of methylthioadenosine. Nat. Commun. *12*, 4228. https://doi.org/10.1038/s41467-021-24240-3.
13. Brennan, C.W., Verhaak, R.G.W., McKenna, A., Campos, B., Noushmehr, H., Salama, S.R., Zheng, S., Chakravarty, D., Sanborn, J.Z., Berman, S.H., et al. (2013). The somatic genomic landscape of glioblastoma. Cell *155*, 462–477. https://doi.org/10.1016/j.cell.2013.09.034.
14. Verhaak, R.G.W., Hoadley, K.A., Purdom, E., Wang, V., Qi, Y., Wilkerson, M.D., Miller, C.R., Ding, L., Golub, T., Mesirov, J.P., et al. (2010). Integrated genomic analysis identifies clinically relevant subtypes of glioblastoma characterized by abnormalities in PDGFRA, IDH1, EGFR, and NF1. Cancer Cell *17*, 98–110. https://doi.org/10.1016/J.CCR.2009.12.020.

15. Guo, D., Prins, R.M., Dang, J., Kuga, D., Iwanami, A., Soto, H., Lin, K.Y., Huang, T.T., Akhavan, D., Hock, M.B., et al. (2009). EGFR signaling through an Akt-SREBP-1-dependent, rapamycin-resistant pathway sensitizes glioblastomas to antilipogenic therapy. Sci. Signal. *2*, ra82. https://doi.org/10.1126/SCISIGNAL.2000446/SUPPL_FILE/2_RA82_SM.PDF.

16. Gimple, R.C., Kidwell, R.L., Kim, L.J.Y., Sun, T., Gromovsky, A.D., Wu, Q., Wolf, M., Lv, D., Bhargava, S., Jiang, L., et al. (2019). Glioma stem cell-specific superenhancer promotes polyunsaturated fatty-acid synthesis to support EGFR signaling. Cancer Discov. *9*, 1248–1267. https://doi.org/10.1158/2159-8290.CD-19-0061.

17. Williams, K.J., Argus, J.P., Zhu, Y., Wilks, M.Q., Marbois, B.N., York, A.G., Kidani, Y., Pourzia, A.L., Akhavan, D., Lisiero, D.N., et al. (2013). An essential requirement for the SCAP/SREBP signaling axis to protect cancer cells from lipotoxicity. Cancer Res. *73*, 2850–2862. https://doi.org/10.1158/0008-5472.CAN-13-0382-T/651001/AM/AN-ESSENTIAL-REQUIREMENT-FOR-THE-SCAP-SREBP.

18. Lita, A., Pliss, A., Kuzmin, A., Yamasaki, T., Zhang, L., Dowdy, T., Burks, C., de Val, N., Celiku, O., Ruiz-Rodado, V., et al. (2021). IDH1 mutations induce organelle defects via dysregulated phospholipids. Nat. Commun. *12*, 614–616. https://doi.org/10.1038/s41467-020-20752-6.

19. Fack, F., Tardito, S., Hochart, G., Oudin, A., Zheng, L., Fritah, S., Golebiewska, A., Nazarov, P.V., Bernard, A., Hau, A.-C., et al. (2017). Altered metabolic landscape in IDH-mutant gliomas affects phospholipid, energy, and oxidative stress pathways. EMBO Mol. Med. *9*, 1681–1695. https://doi.org/10.15252/emmm.201707729.

20. Jain, J.L., et al. (1979). In Fundamentals of Biochemistry (S. Chand & Company), pp. 594–639.

21. Freed-Pastor, W.A., Mizuno, H., Zhao, X., Langerød, A., Moon, S.H., Rodriguez-Barrueco, R., Barsotti, A., Chicas, A., Li, W., Polotskaia, A., et al. (2012). Mutant p53 disrupts mammary tissue architecture via the mevalonate pathway. Cell *148*, 244–258. https://doi.org/10.1016/j.cell.2011.12.017.

22. Bi, J., Ichu, T.-A., Zanca, C., Yang, H., Zhang, W., Gu, Y., Chowdhry, S., Reed, A., Ikegami, S., Turner, K.M., et al. (2019). Oncogene amplification in growth factor signaling pathways renders cancers dependent on membrane lipid remodeling. Cell Metab. *30*, 525–538.e8. https://doi.org/10.1016/j.cmet.2019.06.014.

23. Muranaka, H., Hayashi, A., Minami, K., Kitajima, S., Kohno, S., Nishimoto, Y., Nagatani, N., Suzuki, M., Kulathunga, L.A.N., Sasaki, N., et al. (2017). A distinct function of the retinoblastoma protein in the control of lipid composition identified by lipidomic profiling. Oncogenesis *6*. https://doi.org/10.1038/oncsis.2017.51.

24. Liu, Y., He, Y., Jin, A., Tikunov, A.P., Zhou, L., Tollini, L.A., Leslie, P., Kim, T.H., Li, L.O., Coleman, R.A., et al. (2014). Ribosomal protein-Mdm2-p53 pathway coordinates nutrient stress with lipid metabolism by regulating MCD and promoting fatty acid oxidation. Proc. Natl. Acad. Sci. USA *111*, E2414–E2422. https://doi.org/10.1073/PNAS.1315605111/SUPPL_FILE/PNAS.201315605SI.PDF.

25. Bates, S., Phillips, A.C., Clark, P.A., Stott, F., Peters, G., Ludwig, R.L., and Vousden, K.H. (1998). p14ARF links the tumour suppressors RB and p53. Nature *395*, 124–125. https://doi.org/10.1038/25867.

26. Zhao, R., Choi, B.Y., Lee, M.H., Bode, A.M., and Dong, Z. (2016). Implications of genetic and epigenetic alterations of CDKN2A (p16INK4a) in cancer. EBioMedicine *8*, 30–39. https://doi.org/10.1016/j.ebiom.2016.04.017.

27. Kaiser, H.F. (1958). The varimax criterion for analytic rotation in factor analysis. Psychometrika *23*, 187–200. https://doi.org/10.1007/BF02289233/METRICS.

28. Ayala, A., Muñoz, M.F., and Argüelles, S. (2014). Lipid peroxidation: production, metabolism, and signaling mechanisms of malondialdehyde and 4-hydroxy-2-nonenal. Oxid. Med. Cell. Longev. *2014*, 360438. https://doi.org/10.1155/2014/360438.

29. Bailey, A.P., Koster, G., Guillermier, C., Hirst, E.M.A., MacRae, J.I., Lechene, C.P., Postle, A.D., and Gould, A.P. (2015). Antioxidant role for lipid droplets in a stem cell niche of Drosophila. Cell *163*, 340–353. https://doi.org/10.1016/j.cell.2015.09.020.

30. Dixon, S.J., Lemberg, K.M., Lamprecht, M.R., Skouta, R., Zaitsev, E.M., Gleason, C.E., Patel, D.N., Bauer, A.J., Cantley, A.M., Yang, W.S., et al. (2012). Ferroptosis: an iron-dependent form of nonapoptotic cell death. Cell *149*, 1060–1072. https://doi.org/10.1016/J.CELL.2012.03.042.

31. Eaton, J.K., Furst, L., Ruberto, R.A., Moosmayer, D., Hilpmann, A., Ryan, M.J., Zimmermann, K., Cai, L.L., Niehues, M., Badock, V., et al. (2020). Selective covalent targeting of GPX4 using masked nitrile-oxide electrophiles. Nat. Chem. Biol. *16*, 497–506. https://doi.org/10.1038/s41589-020-0501-5.

32. Dixon, S.J., Winter, G.E., Musavi, L.S., Lee, E.D., Snijder, B., Rebsamen, M., Superti-Furga, G., and Stockwell, B.R. (2015). Human haploid cell genetics reveals roles for lipid metabolism genes in nonapoptotic cell death. ACS Chem. Biol. *10*, 1604–1609. https://doi.org/10.1021/ACSCHEMBIO.5B00245/SUPPL_FILE/CB5B00245_SI_002.PDF.

33. Miotto, G., Rossetto, M., Roveri, A., Venerando, R., Vučković, A.M., Di Paolo, M.L., Bosello-Travain, V., Zaccarin, M., Maiorino, M., Toppo, S., et al. (2018). Insight the mechanism of ferroptosis inhibition by ferrostatin-1. Free Radic. Biol. Med. *120*, S120–S121. https://doi.org/10.1016/J.FREERADBIOMED.2018.04.397.

34. Yang, W.S., Kim, K.J., Gaschler, M.M., Patel, M., Shchepinov, M.S., and Stockwell, B.R. (2016). Peroxidation of polyunsaturated fatty acids by lipoxygenases drives ferroptosis. Proc. Natl. Acad. Sci. USA *113*, E4966–E4975. https://doi.org/10.1073/PNAS.1603244113/SUPPL_FILE/PNAS.1603244113.SD01.XLSX.

35. Kagan, V.E., Mao, G., Qu, F., Angeli, J.P.F., Doll, S., Croix, C.S., Dar, H.H., Liu, B., Tyurin, V.A., Vladimir, B.R., et al. (2017). Oxidized arachidonic and adrenic pes navigate cells to ferroptosis. Nat. Chem. Biol. *13*, 81–90. https://doi.org/10.1038/nCHeMBIO.2238.

36. Dierge, E., Debock, E., Guilbaud, C., Corbet, C., Mignolet, E., Mignard, L., Bastien, E., Dessy, C., Larondelle, Y., and Feron, O. (2021). Peroxidation of n-3 and n-6 polyunsaturated fatty acids in the acidic tumor environment leads to ferroptosis-mediated anticancer effects. Cell Metab. *33*, 1701–1715.e5. https://doi.org/10.1016/J.CMET.2021.05.016.

37. Yen, C.L.E., Stone, S.J., Koliwad, S., Harris, C., and Farese, R.V. (2008). DGAT enzymes and triacylglycerol biosynthesis. J. Lipid Res. *49*, 2283–2301. https://doi.org/10.1194/JLR.R800018-JLR200.

38. Deleye, Y., Cotte, A.K., Hannou, S.A., Hennuyer, N., Bernard, L., Derudas, B., Caron, S., Legry, V., Vallez, E., Dorchies, E., et al. (2020). CDKN2A/p16INK4a suppresses hepatic fatty acid oxidation through the AMPKα2-SIRT1-PPARα signaling pathway. J. Biol. Chem. *295*, 17310–17322. https://doi.org/10.1074/JBC.RA120.012543.

39. Zeng, H., Jorapur, A., Shain, A.H., Lang, U.E., Torres, R., Zhang, Y., McNeal, A.S., Botton, T., Lin, J., Donne, M., et al. (2018). Bi-Allelic loss of CDKN2A initiates melanoma invasion via BRN2 activation. Cancer Cell *34*, 56–68.e9. https://doi.org/10.1016/J.CCELL.2018.05.014.

40. Rabhi, N., Hannou, S.A., Gromada, X., Salas, E., Yao, X., Oger, F., Carney, C., Lopez-Mejia, I.C., Durand, E., Rabearivelo, I., et al. (2018). Cdkn2a deficiency promotes adipose tissue browning. Mol. Metab. *8*, 65–76. https://doi.org/10.1016/J.MOLMET.2017.11.012.

41. Hannou, S.A., Wouters, K., Paumelle, R., and Staels, B. (2015). Functional genomics of the CDKN2A/B locus in cardiovascular and metabolic disease: what have we learned from GWASs? Trends Endocrinol. Metab. *26*, 176–184. https://doi.org/10.1016/J.TEM.2015.01.008.

42. Tsoi, J., Robert, L., Paraiso, K., Galvan, C., Sheu, K.M., Lay, J., Wong, D.J.L., Atefi, M., Shirazi, R., Wang, X., et al. (2018). Multi-stage differentiation defines melanoma subtypes with differential vulnerability to drug-induced iron-dependent oxidative stress. Cancer Cell *33*, 890–904.e5. https://doi.org/10.1016/J.CCELL.2018.03.017.

43. Badgley, M.A., Kremer, D.M., Carlo Maurer, H., DelGiorno, K.E., Lee, H.J., Purohit, V., Sagalovskiy, I.R., Ma, A., Kapilian, J., Firl, C.E.M., et al. (2020). Cysteine depletion induces pancreatic tumor ferroptosis in mice. Science *368*. https://doi.org/10.1126/SCIENCE.AAW9872/SUPPL_FILE/AAW9872S3.MOV.

44. Mai, W.X., Gosa, L., Daniels, V.W., Ta, L., Tsang, J.E., Higgins, B., Gilmore, W.B., Bayley, N.A., Harati, M.D., Lee, J.T., et al. (2017). Cytoplasmic p53 couples oncogene-driven glucose metabolism to apoptosis and is a therapeutic target in glioblastoma. Nat. Med. *23*, 1342–1351. https://doi.org/10.1038/nm.4418.

45. Tannous, B.A. (2009). Gaussia luciferase reporter assay for monitoring biological processes in culture and in vivo. Nat. Protoc. *4*, 582–591. https://doi.org/10.1038/nprot.2009.28.

46. Hsieh, W.Y., Williams, K.J., Su, B., and Bensinger, S.J. (2021). Profiling of mouse macrophage lipidome using direct infusion shotgun mass spectrometry. STAR Protoc. *2*, 100235. https://doi.org/10.1016/J.XPRO.2020.100235.

47. BLIGH, E.G., and DYER, W.J. (1959). A rapid method of total lipid extraction and purification. Can. J. Biochem. Physiol. *37*, 911–917. https://doi.org/10.1139/O59-099.

48. Su, B., Bettcher, L.F., Hsieh, W.-Y., Hornburg, D., Pearson, M.J., Blomberg, N., Giera, M., Snyder, M.P., Raftery, D., Bensinger, S.J., and Williams, K.J. (2021). A DMS shotgun lipidomics workflow application to facilitate high-throughput. J. Am. Soc. Mass Spectrom. *32*, 2655–2663. https://doi.org/10.1021/jasms.1c00203.

49. Williams, K.J., and Bensinger, S.J. (2020). Cellular fatty acid analysis in macrophage using stable isotope labeling. Methods Mol. Biol. *2184*, 47–60. https://doi.org/10.1007/978-1-0716-0802-9_4.

50. Schindelin, J., Arganda-Carreras, I., Frise, E., Kaynig, V., Longair, M., Pietzsch, T., Preibisch, S., Rueden, C., Saalfeld, S., Schmid, B., et al. (2012). Fiji: an open-source platform for biological-image analysis. Nature Methods *9*, 676–682. https://doi.org/10.1038/nmeth.2019.

51. Martin, M. (2011). Cutadapt removes adapter sequences from high-throughput sequencing reads. EMBnet. j. *17*, 10–12. https://doi.org/10.14806/EJ.17.1.200.

52. Bushnell, B. (2014). BBMap: a fast, accurate, splice-aware aligner. In Conference: 9th Annual Genomics of Energy & Environment Meeting.

53. Li, H., and Durbin, R. (2009). Fast and accurate short read alignment with Burrows–Wheeler transform. Bioinformatics *25*, 1754–1760. https://doi.org/10.1093/BIOINFORMATICS/BTP324.

54. Van der Auwera, G.A., and O'Connor, B.D. (2020). Genomics in the Cloud: Using Docker, GATK, and WDL in Terra, 1st ed. (O'Reilly Media).

55. Vivian, J., Rao, A.A., Nothaft, F.A., Ketchum, C., Armstrong, J., Novak, A., Pfeil, J., Narkizian, J., Deran, A.D., Musselman-Brown, A., et al. (2017). Toil enables reproducible, open source, big biomedical data analyses. Nat. Biotechnol. *35*, 314–316. https://doi.org/10.1038/nbt.3772.

56. Dobin, A., Davis, C.A., Schlesinger, F., Drenkow, J., Zaleski, C., Jha, S., Batut, P., Chaisson, M., and Gingeras, T.R. (2013). STAR: ultrafast universal RNA-seq aligner. Bioinformatics *29*, 15–21. https://doi.org/10.1093/BIOINFORMATICS/BTS635.

57. Li, H., Handsaker, B., Wysoker, A., Fennell, T., Ruan, J., Homer, N., Marth, G., Abecasis, G., and Durbin, R.; 1000 Genome Project Data Processing Subgroup (2009). The Sequence alignment/map (SAM) format and SAMtools. Bioinformatics *25*, 2078–2079. https://doi.org/10.1093/bioinformatics/btp352.

58. Benjamin, D., Sato, T., Cibulskis, K., Getz, G., Stewart, C., and Lichtenstein, L. (2019). Calling somatic SNVs and indels with Mutect2. Preprint at bioRxiv. https://doi.org/10.1101/861054.

59. Fan, Y., Xi, L., Hughes, D.S.T., Zhang, J., Zhang, J., Futreal, P.A., Wheeler, D.A., and Wang, W. (2016). MuSE: accounting for tumor heterogeneity using a sample-specific error model improves sensitivity and specificity in mutation calling from sequencing data. Genome Biol. *17*, 178. https://doi.org/10.1186/S13059-016-1029-6/FIGURES/3.

60. Koboldt, D.C., Zhang, Q., Larson, D.E., Shen, D., McLellan, M.D., Lin, L., Miller, C.A., Mardis, E.R., Ding, L., and Wilson, R.K. (2012). VarScan 2: somatic mutation and copy number alteration discovery in cancer by exome sequencing. Genome Res. *22*, 568–576. https://doi.org/10.1101/GR.129684.111.

61. Tate, J.G., Bamford, S., Jubb, H.C., Sondka, Z., Beare, D.M., Bindal, N., Boutselakis, H., Cole, C.G., Creatore, C., Dawson, E., et al. (2019). COSMIC: the catalogue of somatic mutations in cancer. Nucleic Acids Res. *47*, 941–947. https://doi.org/10.1093/nar/gky1015.

62. Chakravarty, D., Gao, J., Phillips, S., Kundra, R., Zhang, H., Wang, J., Rudolph, J.E., Yaeger, R., Soumerai, T., Nissan, M.H., et al. (2017). OncoKB: A Precision Oncology Knowledge Base (JCO Precision Oncology), pp. 1–16. https://doi.org/10.1200/PO.17.00011.

63. Talevich, E., Shain, A.H., Botton, T., and Bastian, B.C. (2016). CNVkit: genome-wide copy number detection and visualization from targeted DNA sequencing. PLoS Comput. Biol. *12*, e1004873. https://doi.org/10.1371/JOURNAL.PCBI.1004873.

64. Ashburner, M., Ball, C.A., Blake, J.A., Botstein, D., Butler, H., Cherry, J.M., Davis, A.P., Dolinski, K., Dwight, S.S., Eppig, J.T., et al. (2000). Gene Ontology: tool for the unification of biology. Nat. Genet. *25*, 25–29. https://doi.org/10.1038/75556.

65. Kanehisa, M., Furumichi, M., Tanabe, M., Sato, Y., and Morishima, K. (2017). KEGG: new perspectives on genomes, pathways, diseases and drugs. Nucleic Acids Res. *45*, D353–D361. https://doi.org/10.1093/NAR/GKW1092.

66. Jassal, B., Matthews, L., Viteri, G., Gong, C., Lorente, P., Fabregat, A., Sidiropoulos, K., Cook, J., Gillespie, M., Haw, R., et al. (2020). The reactome pathway knowledgebase. Nucleic Acids Res. *48*, D498–D503. https://doi.org/10.1093/NAR/GKZ1031.

67. Mi, H., Muruganujan, A., Ebert, D., Huang, X., and Thomas, P.D. (2019). PANTHER version 14: more genomes, a new PANTHER GO-slim and improvements in enrichment analysis tools. Nucleic Acids Res. *47*, D419–D426. https://doi.org/10.1093/NAR/GKY1038.

68. Hanzelmann, S., Castelo, R., and Guinney, J. (2013). GSVA: Gene set variation analysis fro microarray and RNA-Seq Data. BMC Bioinformatics *14*, 7. https://doi.org/10.1186/1471-2105-14-7.

69. Barbie, D.A., Tamayo, P., Boehm, J.S., Kim, S.Y., Moody, S.E., Dunn, I.F., Schinzel, A.C., Sandy, P., Meylan, E., Scholl, C., et al. (2009). LETTERS Systematic RNA Interference Reveals that Oncogenic KRAS-Driven Cancers Require TBK1. https://doi.org/10.1038/nature08460.

70. Love, M.I., Huber, W., and Anders, S. (2014). Moderated estimation of fold change and dispersion for RNA-seq data with DESeq2. Genome Biol. *15*, 550–621. https://doi.org/10.1186/s13059-014-0550-8.

71. R Core Team (2021). R: A Language and Environment for Statistical Computing. https://www.r-project.org/.

72. Cerami, E., Gao, J., Dogrusoz, U., Gross, B.E., Sumer, S.O., Aksoy, B.A., Jacobsen, A., Byrne, C.J., Heuer, M.L., Larsson, E., et al. (2012). The cBio cancer genomics portal: an open platform for exploring multidimensional cancer genomics data. Cancer Discov. *2*, 401–404. https://doi.org/10.1158/2159-8290.CD-12-0095.

73. Gao, J., Aksoy, B.A., Dogrusoz, U., Dresdner, G., Gross, B., Sumer, S.O., Sun, Y., Jacobsen, A., Sinha, R., Larsson, E., et al. (2013). Integrative analysis of complex cancer genomics and clinical profiles using the cBioPortal. Sci. Signal. *6*, 1. https://doi.org/10.1126/SCISIGNAL.2004088.

74. Goldman, M.J., Craft, B., Hastie, M., Repečka, K., McDade, F., Kamath, A., Banerjee, A., Luo, Y., Rogers, D., Brooks, A.N., et al. (2020). Visualizing and interpreting cancer genomics data via the Xena platform. Nat. Biotechnol. *38*, 675–678. https://doi.org/10.1038/s41587-020-0546-8.

75. Wang, Q., Hu, B., Hu, X., Kim, H., Squatrito, M., Scarpace, L., deCarvalho, A.C., Lyu, S., Li, P., Li, Y., et al. (2017). Tumor evolution of glioma-intrinsic gene expression subtypes associates with immunological changes in the microenvironment. Cancer Cell *32*, 42–56.e6. https://doi.org/10.1016/J.CCELL.2017.06.003.

STAR★METHODS

KEY RESOURCES TABLE

REAGENT or RESOURCE	SOURCE	IDENTIFIER
Antibodies		
P16 INK4A (D3W8G) Rabbit mAb	Cell Signaling	Cat# 92803; RRID: AB_2705891
P14 ARF (4C6/4) Mouse mAb	Cell Signaling	Cat# 2407; RRID: AB_490785
GPX4 Mouse mAb	R&D Systems	Cat# MAB5457-SP; RRID: AB_2232542
β-Actin mAb	Cell Signaling	Cat# 3700S; RRID: AB_2242334
Anti-Mouse IgG HRP-linked Antibody	Cell Signaling	Cat# 7076; RRID: AB_330924
Anti-Rabbit IgG HRP-linked Antibody	Cell Signaling	Cat# 7074; RRID: AB_2099233
MDA Goat pAb	Abcam	Cat# ab27644; RRID: AB_776163
Anti-Goat Donkey pAb Alexa Fluor 647	Abcam	Cat# ab150135; RRID: AB_2687955
Bacterial and virus strains		
One Shot Stbl3 Chemically Competent *E. coli*	Invitrogen	C737303
Biological samples		
Patient Derived Brain Tumor Tissue	UCLA Health	N/A
Patient Derived GBM Orthotopic Xenografts	This paper	N/A
Patient Derived GBM Cell Lines (Gliomasheres)	This paper	N/A
Chemicals, peptides, and recombinant proteins		
RSL3	Selleckchem	S8155
Ferrostatin-1	Cayman Chemicals	17729
Liproxstatin-1	Cayman Chemicals	17730
Desferrioxamine (DFO)	Cayman Chemicals	14595
DGAT1 and 2 inhibitors	DGAT1: Santa Cruz Biotechnology DGAT2: Millipore Sigma	DGAT1: 959122-11-3 DGAT2: PZ0233
ML210	Selleckchem	S0788
Arachidonic Acid (AA)	Sigma Aldrich	10931-250mg
Buthionine Sulfoximine (BSO)	Selleckchem	S9728
Erastin2	Cayman Chemicals	HY-139087
Deposited data		
Lipidomics Data (Bulk patient, orthotopic xenograft, gliomasphere, isogenics)	This paper	Mendeley https://doi.org/10.17632/kjtdgk3f25.1
Raw WES fastq (Patient, orthotopic xenograft, gliomaspheres)	This paper	dbGaP (NCBI) Accession: phs003286
Standardized RNA-Sequencing Data (Patient, orthotopic xenograft, gliomasphere)	This paper	dbGaP (NCBI) Accession: phs003286
Patient Lipid Gene Expression-Lipid Species Abundance (Species % Total) Correlation	This paper	Mendeley https://doi.org/10.17632/kjtdgk3f25.1
Experimental models: Cell lines		
Human: 293FT cells	Invitrogen	R7007; RRID: CVCL_6911
Experimental models: Organisms/strains		
Mouse: NOD.Cg-*Prkdc*^{scid} *Il2rg*^{tm1Wjl}/SzJ	The Jackson Laboratory	RRID:IMSR_JAX:005557
Oligonucleotides		
sgRNA targeting sequences for GPX4: See STAR Methods		N/A
shRNA targeting p14/p16		TRCN0000255853
shRNA targeting p14/p16		TRCN0000255849

(*Continued on next page*)

Continued

REAGENT or RESOURCE	SOURCE	IDENTIFIER
Recombinant DNA		
LentiCRISPR v2 plasmid	Addgene	Plasmid 52961 (depositing lab: Feng Zhang); RRID: Addgene_52961
pLKO plasmid	Addgene	Plasmid 10878 (depositing lab: David Root); RRID: Addgene_10878
MISSION® pLKO.1-puro Non-Mammalian shRNA Control Plasmid DNA	Sigma-Aldrich	SHC002
pHIV-ARF-mOrange2	Addgene	Plasmid 110731 (depositing lab: Robert Judson-Torres; RRID: Addgene_110737
pEN35-CDKN2A-Ex2-R	Addgene	Plasmid 110737 (depositing lab: Robert Judson-Torres; RRID: Addgene_110737
pEN35-CDKN2A-Ex2-L	Addgene	Plasmid 110736 (depositing lab: Robert Judson-Torres; RRID: Addgene_110736
pEN35-CKDN2A-Ex2-CMV-EGFP	Addgene	Plasmid 110734 (depositing lab: Robert Judson-Torres
Software and algorithms		
ImageJ Fiji	Schindelin et al. (2012)[50]	https://imagej.net/software/fiji/
Zen Blue 3.4	Zeiss Group	https://www.micro-shop.zeiss.com/en/us/softwarefinder/software-categories/zen-blue/
Prism	GraphPad	https://www.graphpad.com/
BioRender	BioRender	https://biorender.com/
Incucyte	Sartorius	https://www.sartorius.com/en/products/live-cell-imaging-analysis
Samtools (v1.10)	Li et al (2009)[57]	http://www.htslib.org/
CutAdapt (v2.8)	Martin (2011)[51]	https://cutadapt.readthedocs.io/en/stable/installation.html
BBsplit (June 11, 2018)	BBTools (v38.58)	https://www.sourceforge.net/projects/bbmap/
BWA-MEM (0.7.17-r1188)	Li and Durbin (2009)[52]	https://github.com/lh3/bwa
GATK (v4.2.0.0)	Broad Institute	https://gatk.broadinstitute.org/hc/en-us
Seal	BBTools (v38.58)	https://www.sourceforge.net/projects/bbmap/
Toil RNA-Seq (v3.3.5)	Vivian et al. 2017[55]	https://github.com/BD2KGenomics/toil-rnaseq
Mutect2 v4.2.0.0	Broad Institute	https://gatk.broadinstitute.org/hc/en-us/articles/360056969692-Mutect2
VarScan2 (v2.4.3)	Koboldt et al. (2012)[60]	https://varscan.sourceforge.net/
MuSE v1.0rc	MD Anderson Cancer Center	https://bioinformatics.mdanderson.org/public-software/muse/
CNVkit (v0.99)	Talevich et al. (2016)[63]	https://cnvkit.readthedocs.io/en/stable/
R (v4.1.0)	CRAN	https://www.r-project.org
GSVA (v1.40.1)	Hanzelmann et al. (2013)[68]	https://bioconductor.org/packages/release/bioc/html/GSVA.html
EnrichR	Ma'ayan Lab	https://maayanlab.cloud/Enrichr/
Gene Ontology (GO) Resource	Ashburner et al. (2000)[64]	http://geneontology.org/
Kyoto Encylclopedia of Genes and Genomes (KEGG)	Kanehisa Laboratories	https://www.genome.jp/kegg/
Reactome	Jassal et al, 2020[66]	https://reactome.org/
STAR	Dobin et al. (2013)[55]	https://github.com/alexdobin/STAR
RSEM	Li et al. (2011)[56]	https://deweylab.github.io/RSEM/
Other		
ProLong Gold antifade reagent with DAPI	Invitrogen	P36935
HCS LipidTOX™ Deep Red neutral lipid dye	Invitrogen	H34477
CellTOX cell death green fluorescent dye	Promega	G8741
Incucyte nuclear red fluorescent dye	Sartorius	4717

(*Continued on next page*)

Continued

REAGENT or RESOURCE	SOURCE	IDENTIFIER
C11 BODIPY 581/591	Thermo Scientific	D3861
Hoechst nuclear stain	Thermo Scientific	62249
Tumor dissociation kit, human	Miltenyi Biotec	130-094-929
Brain Tumor Dissociation Kit (P)	Miltenyi Biotec	130-095-942
Mouse Cell Depletion Kit	Miltenyi Biotec	130-104-694
Myelin Removal Beads II, h&m&r, 2x4ml	Miltenyi Biotec	130-096-433
CD45 MicroBeads, human	Miltenyi Biotec	130-045-801
Debris Removal Solution	Miltenyi Biotec	130-109-398
Laminin, Mouse	Corning	354232
Heparin sodium salt from porcine intestinal mucosa	Sigma	H3149
Gibco FGF-Basic (AA 1-155) Recombinant Human Protein	Thermo Scientific	PHG0263
Gibco EGF Recombinant Human Protein	Thermo Scientific	PHG0313
Gibco TrypLE Express Enzyme (1X), phenol red	Thermo Scientific	12605028
Gibco DMEM/F-12, HEPES	Thermo Scientific	11330032
Gibco DMEM, high glucose, pyruvate, no glutamine	Thermo Scientific	10313039
Mycoalert Detection Kit	Lonza	LT07-318
BenchMark™ Fetal Bovine Serum	Gemini Bio	100-106-500

RESOURCE AVAILABILITY

Lead contact

Further information and requests for resources and reagents should be directed to and will be fulfilled by the lead contact, David Nathanson (dnathanson@mednet.ucla.edu).

Materials availability

This study did not generate new unique reagents.

Data and code availability

Whole exome sequencing has been deposited at the database of Genotypes and Phenotypes (dbGaP) and is publicly available as of the date of publication. Accession numbers are listed in the key resources table. RNA-seq data has been deposited at dbGaP and is publicly available as of the date of publication. Accession numbers are listed in the key resources table. Shotgun lipidomics data has been deposited at Mendeley and is publicly available as of the date of publication. Accession numbers are listed in the key resources table. Lastly, the data generated in Figure 1C (Lipid-Gene Correlation Matrix) has been deposited to Mendeley and is publicly available as of the date of publication. The DOI is listed in the key resources table.

- This paper does not report original code.
- Any additional information required to reanalyze the data reported in this paper is available from the lead contact upon request.

EXPERIMENTAL MODEL AND SUBJECT DETAILS

Patient-derived GBM tumors and gliomaspheres

After explicit informed consent was obtained from patients, all patient-derived tumor tissue was obtained through the UCLA Institutional Review Board (IRB) protocol 10-000655. Sample size for shotgun lipidomics, RNA-seq, and WES were determined based on tissue availability. Patient sex for all derivative samples and models are annotated in Figure 1B. Tumors were mechanically and enzymatically dissociated using the Miltenyi Biotec Human tumor dissociation kit. Red blood cell lysis buffer removed red blood cells. Antibody-conjugated magnetic beads removed $CD45^+$ cells and myelinated cells in two column-based filtration steps. Primary GBM cells were established and maintained in gliomasphere conditions consisting of DMEM/F12 (Gibco), B27 (Invitrogen), penicillin–streptomycin (Invitrogen), and GlutaMAX (Invitrogen) supplemented with heparin (5 μg/mL, Sigma), EGF (20 ng/mL, Sigma), and FGF (20 ng/mL, Sigma). All cells were grown under 37 °C, 20% O2, and 5% CO2 and were routinely monitored and tested negative for the presence of mycoplasma with a commercially available kit (MycoAlert, Lonza). Gliomasphere cell lines were used at fewer than 15 passages. All cells were authenticated by short tandem repeat (STR) analysis.

Mice

Female, immunocompromised NOD scid gamma (NSG) mice, 6–8 weeks of age, were purchased from the University of California Los Angeles (UCLA) Medical Center animal-breeding facility and Jackson Laboratories. All mice were kept under defined pathogen-free

conditions at the AAALAC-approved animal facility of the Division of Laboratory Animals (DLAM) at UCLA. Mice did not receive any prior treatments and were drug and test naïve prior to injection of tumor cells. All animal experiments were performed with the approval of the UCLA Office of Animal Resource Oversight (OARO).

Patient-derived orthotopic xenografts

The majority of the patient-derived orthotopic xenografts (*n*=27) were developed as previously described.[44] Briefly, gliomaspheres were transduced with secreted *Gaussia* luciferase (sGluc)-GFP reporter to enable non-invasive quantification of tumor burden[45] as well as endpoint GFP-guided microdissection of the tumor tissue from the surrounding normal brain. Gliomaspheres were dissociated and injected (5 x10^5 cells per injection) into the right striatum of the brain in female NSG mice (8-9 weeks old). Injection coordinates were 2 mm lateral and 1mm posterior to bregma, at a depth of 2mm. For two models, PDX074 and PDX152, freshly isolated and purified patient tumor cells were transduced with sGluc and 5 x 10^5 cells and inoculated into the brains of mice per the same protocol as gliomaspheres implantation.

Tumor burden was monitored based on 1-2x weekly measurements by sGluc. Upon endpoint, mice were euthanized and tumors were dissected from the brains. The isolated tumor tissue was then submitted for shotgun lipidomics analysis. For WES and RNA-seq analysis, tumor cells were purified via mechanical and enzymatic dissociation using the Miltenyi Biotec Mouse tumor dissociation kit. Antibody-conjugated magnetic beads removed myelinated and mouse cells in a two column-based filtration step. Sample size for shotgun lipidomics, RNA-seq, and WES were determined based on model availability. For *in vivo* studies involving genetically manipulated tumors (see Figure 6), sample size was estimated based on previous studies.

METHOD DETAILS

Secreted *Gaussia* luciferase measurements

Cells were infected with a lentiviral vector containing a secreted *Gaussia* luciferase (sGluc)-encoding reporter gene (Targeting Systems no. GL-GFP) and intracranially implanted into the right striatum in mice (4 × 10^5 cells/mouse). To measure the levels of sGluc, 6 μL of blood was collected from the tail vein and immediately mixed with 50 mM EDTA to prevent coagulation. sGluc activity was obtained by measuring chemiluminescence after injection of 100 μL of 100 μM coelentarazine (Nanolight) in a 96-well plate, as described before.[45]

Genetic manipulations

Lentivirus particles used for genetic manipulation were produced by transfection of 293-FT cells (Thermo) with Lipofectamine 2000 (Invitrogen). Virus particles were collected 48 h after transfection. The *CDKN2A* shRNA guide sequences used to knockdown p14 and p16 TRCN0000255853 and TRCN0000255849 in the Vector backbone pLKO (Addgene, plasmid 10878). Mission pLKO.1-puro Non-Mammalian shRNA Control (Sigma-Aldrich, SHC002) was used as the shRNA scramble control (shC). GPX4 CRISPR-Cas9 gene disruption was performed with the LentiCRISPR V2 vector (Addgene, plasmid 52961) using the following oligonucleotide sequences:

	Forward (5' > 3')	Reverse (5' > 3')
sg*GPX4*-1	caccgttaacctggacaagtaccgg	aaacccggtacttgtccaggttaac
sg*GPX4*-2	caccgtgcacgagttttccgccaag	aaaccttggcggaaaactcgtgcac
sg*GPX4*-3	caccgaagtaaactacactcagctc	aaacgagctgagtgtagtttacttc

Cells were spinfected with lentivirus generated from LentiCRISPR V2 non-targeting (NT) control, sg*GPX4*-1, sg*GPX4*-2, or sg*GPX4*-3 (500 uL lentivirus, 1 million cells plated in 1 mL media in a 6-well plate, 1 ug/mL Polybrene) at 800g for 1 hour and 30 minutes (32C). Cells were immediately transferred into normal gliomasphere media and subjected to puromycin selection (1μM puromycin). Post-spinfection, cells were continuously cultured in 1μM ferrostatin-1 (refreshed every 2-3 days) until experimentation or implantation into mice.

CRISPR-Cas9 mediated *CDKN2A* disruption, as well as addback of p16, were performed as previously described.[39] Cells were infected with pEN35-CDKN2A-Ex2-R, pEN35-CDKN2A-Ex2-L, and pHDR-CDKN2A-Ex2-CMV-EGFP cDNA (1 ug of cDNA per construct per 1,000,000 cells). Cells were allowed to expand and were then sorted via FACS isolation. After validation of CDKN2A knock-out with Western blotting, cells were then infected with pHIV-INK4A-mOrange2 cDNA (1 ug of cDNA per 1,000,000 cells), expanded, and then sorted via FACS isolation.

Immunoblotting

Cells were collected and lysed in RIPA buffer (Boston BioProducts) containing Halt Protease and Phosphatase Inhibitor (Thermo Fisher Scientific). Lysates were centrifuged at 14,000 x g for 15 min at 4°C. Protein samples were then boiled in NuPAGE LDS Sample Buffer (Invitrogen) and NuPAGE Sample Reducing Agent (Invitrogen), separated with SDS–PAGE on 12% Bis-Tris gels (Invitrogen)

and transferred to nitrocellulose membranes (GE Healthcare). Immunoblotting was performed per the antibody manufacturers' specifications, as mentioned previously. Membranes were developed with the SuperSignal system (Thermo Fisher Scientific).

Exogenous fatty acid addition – shotgun lipidomics

For Figure 4A, cells were plated at a density of 5 million cells in 50 mL media and treated with the following conditions (in triplicate) for 24 hours prior to collection for shotgun lipidomics analysis: Vehicle (DMSO), 75 μM arachidonic acid (AA), or 20 μM DGAT1 inhibitor+10 μM DGAT2 inhibitor+75 μM AA for 24 hours.

Shotgun lipidomics

After removal of cell culture media, cells were resuspended in 200 uL of ice-cold PBS and collected in glass tubes. Samples were prepared for shotgun lipidomic analysis at the UCLA Lipidomics Core (detailed protocol published by Hsieh W.Y. et al).[46] In short, a modified Bligh and Dyer extraction was performed on all samples.[47] Prior to extraction, a 13-class lipid class Lipidizer Internal Standard (AB Sciex, 5040156) was added to each sample. After two extractions, the pooled organic layers were dried down in a Genevac EZ-2 Elite, and lipid samples were resuspended in 1:1 methanol/dichloromethane with 10 mM Ammonium Acetate. Samples were analyzed on the Sciex Lipidyzer Platform for targeted quantitative measurement of 1100 lipid species across 13 classes. Differential Mobility Device on Lipidyzer was tuned with SelexION tuning kit (Sciex 5040141). Instrument settings, tuning settings, and MRM list available upon request. Data analysis was performed according to the workflow published by Su, B. et al (2021).[48]

Annotating lipid species characteristics

For results examining acyl tail characteristics of lipid species, monoacyl species were annotated based off their one fatty acyl tail (e.g., LPC 14:0 – carbon number: 14; number of double bonds: 0). Diacyl species were annotated based off their two fatty acyl tails (e.g., DG18:0_18:3 counted as two different acyl tails, one with 18 carbons and 0 double bonds, and another with 18 carbons and 3 double bonds). Triacyl species are fragmented into multiple species, with each species representing a different acyl tail, and were annotated based off their one detectable fatty acyl tail per species (e.g., TG 49:2-16:1 counted as having one acyl tail with 16 carbons and 1 double bond). For results examining lipids at the molecular species level, TAG length and double bond numbers were based on the single detected tail and saturation was determined based on information on both the number of double bonds on the detected tail and total number of double bonds detected across all three tails (e.g., TG52:5-16:0 counted as PUFA because there must be at least two double bonds on one of the other acyl tails). For results examining TAG species characteristics, double bonds and total carbons were determined by looking at the overall number of double bonds and overall number of carbons present in the TAG species.

Fatty acid analysis

Fatty Acid analysis was carried out as described previously.[49] Briefly, cells were collected and counted for normalization. Nonadecanoic methyl ester internal standard (N-19-M, Nu-Chek Prep) was added to derivatization mixture. Total fatty acids methyl esters were prepared by acid methanolysis reaction carried out for 12-16 hours at 45C. Resulting FAMEs were extracted in hexane. Samples were analyzed with an Agilent 7890B/5977A GC-MS using a 30m UI-DB-WAX column (Agilent 122-7032UI). GC oven and MSD settings available upon request. Fatty acids were identified by retention time and parental ion m/z. Relative amounts were normalized to internal standard.

Quantifying lipid peroxidation with BODIPY 581/591 C11

Lipid peroxidation was assessed using the lipid peroxidation probe C11 BODIPY 581/591 from Thermo Fisher (D3861). To assess lipid peroxidation *in vitro*, gliomaspheres (non-GFP transduced) were split and cultured for 24 h in previously described gliomasphere medium except the B-27 supplement is without antioxidants (Gibco, 10889038). After 24 h, the cells were collected, dissociated with trypsin, and re-suspended as single cells in Hank's Buffered Salt Solution (HBSS) containing the C11 BODIPY 581/591 (1:1000) and Hoechst nuclear stain (1:1000). Cells were incubated for 15 minutes in the dark in solution on a Cell-tak treated coverslip to enable cell adhesion. Coverslips were then washed once in HBSS and inverted onto a slide with 100 μl HBSS and parafilm spacers, and then sealed with Valap to enable live cell confocal microscopy. Images were acquired on a confocal LSM880 microscope at 63x magnification to capture DAPI (405/462), non-oxidized C11 (594/667), and oxidized C11 (488/554). Quantification was performed as follows: .czi files were opened in ImageJ FIJI[50] and the red and green channels were merged. ROIs were drawn around 30 representative cells, and values were generated on a cell-by-cell basis for both red and green channels. Oxidation was quantified as (green average intensity)/ (red average intensity+green average intensity). Representative images were generated by merging red, green, and blue channels in ImageJ and adjusting brightness/contrast for visualization (same parameters applied to all images being compared to one another).

Cell death kinetics – Incucyte

Opaque-sided clear bottomed 96-well plates or 384-well plates were laminin-coated for 1 hour and then washed two times with neurobasal media. Gliomaspheres were dissociated into single cell suspension, filtered, plated at 20,000 cells per well (96-well) or 5,000 cells per well (384-well), and allowed to attach for 4 to 12 h. Once cells were attached, media was briefly removed and replaced with medium containing antioxidant-free B27 and CellTOX cell death green fluorescent dye (1:1000) (Promega, G8741) and nuclear red

fluorescent dye (1:1000) (Sartorius, 4632) as well as the required compounds. The plate was then set in an Incucyte live-cell imaging system (Sartorius) which acquires images every 2 h for up to five days. Incucyte software image analysis was performed using top-hat image normalization (Satorius Incucyte User Manual), and percent cell death was calculated using percentage of green objects/mm^2 over red objects/mm^2.

Cell death kinetics – Trypan blue exclusion

Gliomaspheres were dissociated into single cell suspension, filtered, and plated at 200,000 cells per well in a 12-well plate. Cells plated in triplicate per condition in DMEM/F12+antioxidant free B27+glutamax+Pen/strep with either DMSO vehicle or 2.5μM RSL3. After 72 hours, cells were collected, split with TrypLE for 3 minutes, and resuspended in 1 mL media. Cells were then counted with the Countess 3 Automated Cell Counter at a 1:1 ratio of trypan blue: cell suspension. Brightfield was used to capture total cell count, Dead Cells (%), and Live Cells (%).

Quantifying MDA levels with immunofluorescent microscopy - Tissue

Tumor tissues were fixed in 4% PFA and paraffin-embedded, and slices were mounted onto slides. Slides were incubated at 60C for 30 min, then deparaffinized in xylene (100%, 3x5 min). Slides were then rehydrated in graded alcohols (100%, 100%, 95%, 80%, 70%, 50%, 2 min each). Antigen retrieval was performed in antigen retrieval solution (100 mM Tris, 5% (w/v) urea, pH 9.5). Blocking was done with 10% BSA in TBST for 5 minutes. Slides were incubated overnight at 4°C with 1:500 goat anti-MDA primary antibody (Abcam ab27644) followed by secondary incubation with 1:1000 donkey anti-goat Alexa 647 (Abcam ab150131). Coverslips were mounted to the slides using the ProLong Gold antifade reagent with DAPI (Invitrogen, P36935). Confocal microscopy on the LSM880 microscope at 20x magnification was used to capture tissue sections (MDA (633/697), GFP (488/546), and DAPI (405/498)). Average intensity of MDA was quantified in ImageJ Fiji,[50] and images were converted to JPEG files using the Zen Blue software. To quantify MDA intensity, the threshold was set based off of a representative, high MDA image. This threshold was then used for all images being compared to one another. For image visualization, the Alexa-647 far red channel was changed to orange.

Quantifying MDA levels with immunofluorescent microscopy - Cells

Cells were plated at a density of 200K per well in a 12-well plate and incubated for 24 hours in DMEM/F12+glutamax+P/S+B27 without antioxidants. Cells were collected, pelleted, washed with PBS, pelleted, then resuspended in 100 uL PBS and added to Cell-Tak'd coverslips. After 1 hour, cells were fixed with 4% PFA and incubated for an additional 15 minutes. PFA was washed three times with PBS and were permeabilized with 0.5% Triton X-100 in PBS. After 15 minutes, cells were washed three times with PBS and were blocked with 10% BSA in PBS for an hour. After blocking, cells were washed three times with PBS and incubated in primary antibody overnight at 4C (goat anti-MDA primary antibody diluted 1:500 in 1% BSA in PBS). The next day, cells were washed three times with PBS to remove primary antibody. Cells were then incubated for 1 hour in the dark with secondary antibody (donkey anti-goat Alexa-647 secondary antibody diluted 1:1000 in 1% BSA in PBS). Cells were washed three times with PBS to remove excess secondary, washed one time with distilled water to remove PBS, then mounted to slides with ProLong Gold antifade reagent with DAPI. Confocal microscopy on the LSM880 microscope at 60x magnification was used to capture at least 30 cells (MDA (633/697), GFP (488/546), and DAPI (405/498)). Average intensity of MDA was quantified in ImageJ Fiji,[50] and images were converted to JPEG files using the Zen Blue software. To quantify MDA intensity, the threshold was set based off a representative, high MDA image. This threshold was then used for all images being compared to one another. For image visualization, the Alexa-647 far red channel was changed to orange.

Lipid droplet imaging and quantification

Lipid droplets were assessed using HCS LipidTOX™ Deep Red neutral lipid dye. Cells were collected and trypsinized following standard procedure for gliomasphere cultures. The cell pellet was then re-suspended in media containing the LipidTOX™ dye (1:1000). Cells were distributed onto a coverslip pre-treated with Cell-tak to enable rapid cell adhesion. Cells were allowed to attach to the coverslip for 30 min before the addition of 4% PFA to fix the cells. Coverslips were washed in HBSS and then water and mounted onto a slide using Invitrogen Prolong Gold Antifade mounting reagent with DAPI. Confocal microscopy on the LSM880 microscope at 63x magnification was used to capture the lipid droplet (488/563) and DAPI (405/453). Lipid droplet area and number per cell was quantified using ImageJ FIJI.[50] To quantify lipid droplet area, the threshold was set based off of a representative, high LD image (only masking punctate signal). This threshold was then used for all images being compared to one another. Particles were then analyzed, summed per image, then divided by the number of cells (at least 30 cells) captured in that image. For image visualization, the color of the far-red channel was switched to green on ImageJ, and the far red and blue channels were merged into a composite image.

Whole exome and RNA sequencing

Prior to January 21st 2021, whole exome libraries were prepared using the SeqCap EZ Human Exome Library V3 kit and sequenced on the Illumina HiSeq 3000 or Novaseq 6000 systems (paired-end, 150bp). Afterwards, libraries were constructed using the KAPA HyperExome enrichment kit and sequenced on the NovaSeq 6000 system. On average, 120-fold (100∼150 fold) exome-wide target coverage was achieved for all sequenced tumor and normal blood and peripheral blood mononuclear cell (PBMC) samples. Transcriptome libraries were constructed from poly(A) selected RNA using the Nugen Universal Plus mRNA-seq library prep kit and

sequenced on the HiSeq 3000 or Novaseq 6000 systems (paired-end, 150bp). Gliomas were RNA sequenced and achieved an average read depth of approximately 35 million mapped deduplicated reads per sample.

Whole exome QC and mapping

For WES, adapter trimming was performed with Cutadapt,[51] with minimum read length after trimming 20 and mean quality value before trimming of 20. To remove potential mouse contamination from sequenced library, we mapped trimmed reads to mouse (mm10) and human (GRCh38) genomes simultaneously with BBsplit from the BBtools package.[52] After removing contaminant and ambiguous reads, alignment to the hg38 human reference genome was carried out with BWA 0.7.17-r1188.[53] We followed GATK v4.2.0.0 best practices to mark duplicate reads and perform base quality score recalibration with ApplyBQSR.[54]

RNA-seq QC and mapping

For RNA sequencing, reads unambiguously aligning to the mouse genome were removed with the same mapping strategy as for WES, using Seal from the BBtools package. Filtered reads were then processed through the UCSC Toil RNA sequencing pipeline[55] for quality control, adapter trimming, sequence alignment, and expression quantification. Briefly, sequence adapters are trimmed and sequences are then aligned to human reference genome (GRCh38) using STAR v2.4.2a[56] and gene expression quantification is performed using RSEM v1.2.25.[57] Expression values are output as raw counts and transcripts per million (TPM) for downstream analysis.

Somatic mutation and copy number alteration calling

For tumor samples with a sequenced matched normal, Mutect2 v4.2.0.0[58] MuSE v1.0rc,[59] and Varscan2[60] were used to call mutations. To avoid potential false positive variants, variants with minimum coverage of 20 reads and identified by at least two mutation callers were selected for further analysis. For samples without matched normal sequencing, variants were called using Mutect2 in tumor-only mode. Variants were compared against the matched normal sample when available, as well as a constructed panel of normal samples following GATK best practices. Variants were then filtered based on occurrence frequency in COSMIC database[61] (>7 occurrences in CNS tumors) or annotated as "likely oncogenic" or "oncogenic" by OncoKB.[62] CNVkit was used to detect copy number changes from whole-exome sequencing data.[63]

EGFR^{vIII} calls were generated based on alternative transcript splicing of *EGFR* detected in RNA sequencing data. *EGFR*^{vIII} calls were determined by calculating the fraction of reads mapping to the junction between exons 7 and 8 and the aberrant junction between exons 1 and 8 (indicative of an in-frame deletion of exons 2-7) to generate *EGFR*^{vIII} transcript allele frequencies (TAFs). Samples with TAFs > 10% were considered positive for *EGFR*^{vIII} variant.

Integrated *CDKN2A* status based on whole exome and RNA sequencing

To generate a final call of *CDKN2A* status for all patient tumors, we combined information from our whole exome and RNA sequencing pipelines. First, segment level copy number values were manually reviewed for consistency with copy number ratios calculated within each 5 kilobase window overlapping *CDKN2A*. Cases with discordant bin-level and segment-level copy number estimates were manually adjusted based on the average of bins. Patient tumor samples with *CDKN2A* deep deletions based on WES were typed as *CDKN2A* null. Samples with *CDKN2A* shallow deletions or diploid copy number based on WES combined with greatly decreased *CDKN2A* RNA expression ($\log_2$ TPM < 2.5) and copy number deletions detected in their matched patient-derived models were typed as *CDKN2A* null. All other samples with shallow deletions, diploid copy number, or copy number gains of *CDKN2A* based on WES without further evidence of deletion were *CDKN2A* wild type.

Lipidome-transcriptome correlation analysis

For patient tumors, matched lipidomic profiling (% of total, n=918 species overlapping in patient and gliomasphere profiling) and gene expression data ($\log_2$ TPM+1) from 84 patient tumor samples were integrated to evaluate relationships between variation in gene expression and lipid composition. Gene expression data were filtered to genes annotated in a Gene Ontology, KEGG, or Reactome term related to lipid metabolism with average expression above 0.5 $\log_2$ TPM+1 (n = 999).[64–66] Pearson's correlation coefficients were then calculated for each lipid-gene pair. Correlation values were hierarchically clustered based on Euclidean distance using Ward's method. Clusters of lipids and genes were defined using static tree cutting of hierarchical clustering results.

For gliomaspheres, lipidomic profiling (% of lipid class, n=985 species) and gene expression data ($\log_2$ TPM+1) from 43 samples were used. Gene expression data were first filtered to protein coding genes with average expression above 0.5 $\log_2$ TPM+1. Genes and lipids were further filtered to remove the bottom 20% and 10% of low variance features respectively (10,778 remaining genes, 835 remaining lipid species). Pearson's correlation coefficients were then calculated and the top 25% of genes (n=2,695 genes) with most variable correlation values were selected for downstream analysis and plotting based on their ability to preserve patterns observed globally.

Correlation cluster annotation and lipid-gene cluster co-enrichment

Lipid clusters defined in the patient lipid-gene correlation analysis were annotated based on their enrichment for specific lipid classes, saturation levels, and chain length categories based on hypergeometric p-values calculated through comparison of each cluster to the background of all analyzed lipid species. Hypergeometric p-values for each category were adjusted using the

Benjamini-Hochberg procedure. Gene clusters were annotated with their enriched lipid metabolic features based on geneset over-representation analysis run on Gene Ontology Biological Process (GO BP) terms using the PANTHER Classification System.[67] GO BP results were filtered to terms involved in the metabolism or biosynthesis of detectable lipid classes (i.e. excluding terms including "negative regulation" or "catabolism") with adjusted p-value < 0.05 and then sorted based on fold enrichment to identify enriched lipid metabolic terms.

Co-enrichment scores quantifying the relationships between pairs of lipid and gene clusters were calculated based on the average of two two-sample Kolmogorov-Smirnov statistics: one statistic calculated on genes ranked based on their correlation with lipids of a given lipid cluster, and another statistic calculated on lipids ranked based on their correlation with genes of a given gene cluster. The first statistic quantifies the specificity of gene cluster correlations for each lipid cluster while the second statistic quantifies the specificity of lipid cluster correlations for each gene cluster. P-values were adjusted using the Benjamini-Hochberg procedure and cluster pairs with adjusted p-values < 0.05 for both gene-wise and lipid-wise enrichment as well as congruent directionality (positive or negative enrichment) were deemed significant co-enrichment results.

Genetic alteration - lipid cluster enrichment scoring

To quantify whether lipid species in each lipid cluster are enriched positively or negatively with a given genetic alteration, a log odds ratio was calculated between the fraction of significantly over-abundant lipid species within a lipid cluster and the fraction of significantly under-abundant lipid species within the same cluster (Student's t-test p-value < 0.05). Fisher's exact test, with Haldane-Anscombe correction (adding 0.5 to each cell to avoid zeroes), was carried out on counts of the significantly different lipid species inside or outside of a given lipid cluster for a given genetic alteration. This test was performed for each pair of lipid clusters and genetic alterations and p-values were adjusted using the Benjamini-Hochberg procedure.[68]

Gene cluster scoring and genomic association testing

Single sample GSEA (ssGSEA)[69] was used to score individual samples for their enrichment for gene sets defined in correlation analyses in patient tumors and gliomaspheres. For gliomaspheres, a composite score was defined as the difference between the enrichment scores for the two gene clusters and was used to test for associations with genomic alterations.

For genome-wide testing, gene-level copy number amplifications (8+ copies), deep deletions (< 0.5 copies), and somatic mutations detected via WES were individually considered for testing. For each gene, samples were grouped by their binary alteration status and Welch's t-test was used to quantify their association with ssGSEA composite scores. Gene-level results for somatic amplifications and deletions were then clustered into locus-level results by grouping genes with genomic coordinates within 1 Megabase of each other and taking the most extreme test statistic from the set of clustered genes to represent the locus. Locus-level results for amplifications and deletions were then merged with gene-level results for point mutations and p-values were adjusted using the Benjamini-Hochberg procedure.

Differential expression analysis

Differential gene expression analysis was carried out using DESeq2 on expected count data from RSEM rounded to whole numbers.[70] Genes were pre-filtered to remove genes with average counts below 100. Fold change estimates were shrunken using the adaptive shrinkage option *lfcShrink(..., type = "ashr")* provided in DESeq2.[70]

Principal component analysis and varimax rotation

Principal component analysis (PCA) was carried out using the *prcomp()* function in R v4.1.0 without scaling features.[71] PCA loadings for PC1 and PC2 were then rotated using varimax rotation without Kaiser normalization using the R package varimax.[27] Rotated component scores were calculated by multiplying the original PC scores by the varimax rotation matrix.

Differential lipid abundance permutation analysis

To determine the statistical significance of differential lipid abundance results obtained using Student's t-test, permutation analysis was performed by randomly shuffling the group labels without replacement and re-running the differential lipid abundance testing 100,000 times. The number of differentially abundant lipids were then counted for various significance levels (α = [0.25, 0.15, 0.05, 0.01, 0.001]) and quantiles of the permutation results (median, top 10%, top 5%, top 1%) for comparison to the observed number of differentially abundant lipids at the same significance levels. A final permutation p-value was calculated as the fraction of random permutations with equal or more significantly different lipid species than the observed result at $\alpha = 0.05$.

TCGA GBM multi-omics data and analysis

Somatic point mutations and copy number alterations for TCGA GBM samples was accessed through CBioPortal (Glioblastoma, *Cell* 2013).[13,72,73] Gene expression results from RSEM were accessed from the Toil RNA-seq Recompute[55] project publicly available through UCSC XenaBrowser.[74] Datasets were then filtered to only include samples present in all datasets (n = 142).

Samples were then scored for their enrichment for each gene cluster defined in the patient correlation analysis using ssGSEA. ssGSEA scores were then stratified by *CDKN2A* alteration status (defined as either deletion or somatic mutation with loss of heterozygosity) and statistical testing was performed using Welch's t-test for both our cohort and TCGA GBM.

Gene expression subtyping

Tumors from patients with GBM, orthotopic xenografts, and gliomasphere cultures were scored for their enrichment of previously defined TCGA GBM subtypes using ssGSEA.[75] An empirical distribution of expected ssGSEA scores for each subtype signature were generated from permutations of the patient tumor expression values generating 1 million simulated ssGSEA scores per subtype. These simulated distributions were used to convert observed ssGSEA scores into permutation z-scores and empirical p-values indicating significance of subtype enrichment as done previously.[75] In cases where a sample showed enrichment for multiple subtypes, the sample was called based on its maximum z-score.

QUANTIFICATION AND STATISTICAL ANALYSIS

Comparisons were made with two-tailed unpaired Student's t-tests, and unless otherwise stated, unadjusted p-values <0.05 were considered statistically significant. Welch's t-test was used when comparison groups were observed to have disparate variances. No further statistical methods or tests assessing the distribution of the data were used. All data from multiple independent experiments were assumed to be t-distributed. For each experiment, replicates are as noted in the figure legends. Data represent mean ± s.d. values unless otherwise indicated in the figure legends. All statistical analyses were calculated in Prism 9.0 (GraphPad). Sample size was selected based on previous studies. No samples were excluded. For all figures: $p > 0.05$ = ns; $p < 0.05$ = *; $p < 0.01$ = **; $p < 0.001$ = ***; $p < 0.0001$ = ****.